IEEE Access
Multidisciplinary | Rapid Review | Open Access Journal

Received 3 December 2024, accepted 6 February 2025, date of publication 10 February 2025, date of current version 13 February 2025.

Digital Object Identifier 10.1109/ACCESS.2025.3540316

RESEARCH ARTICLE

A Deterministic Method for Contactless Monitoring of Vital Signs Using Multiple FMCW Radars in the 24 GHz Band

ELIA VIGNOLI[1], (Graduate Student Member, IEEE), PASQUALE DI VIESTI[1,2], (Member, IEEE), AND GIORGIO MATTEO VITETTA[1,2], (Senior Member, IEEE)

[1]Department of Engineering "Enzo Ferrari," University of Modena and Reggio Emilia, 41124 Modena, Italy
[2]Consorzio Nazionale Interuniversitario per le Telecomunicazioni, 43124 Parma, Italy

Corresponding author: Elia Vignoli (elia.vignoli@unimore.it)

The technical content of this manuscript is patent pending.

ABSTRACT In this manuscript, the problem of estimating human vital signs through a plurality of single-input multiple-output frequency modulated continuous wave radars is investigated. A novel algorithm for real-time estimation of heart rate and respiration rate, and for apnea detection is developed. It employs a selection combining technique and a filtering method inspired by Bayesian filtering principles. Our experimental results evidence that the proposed algorithm, tested on commercial radar devices, outperforms well known vital signs estimation methods available in the technical literature at the price of a limited increase in computational complexity.

INDEX TERMS Biomedical engineering, biomedical signal processing, electronic healthcare, millimeter wave radar, radar remote sensing, signal denoising.

I. INTRODUCTION

Over the last two decades, substantial attention has been devoted to the development of accurate methods for contactless *vital sign monitoring* (VSM) of human beings and, in particular, for the monitoring of *heart rate* (HR) and *breath rate* (BR) [1], [2], [3]. This interest is motivated by the fact that, in various circumstances (e.g., when dealing with infected patients or individuals experiencing mental health issues or people afflicted by extensive burns or injuries), the use of wearable sensors or traditional monitoring methods like *electrocardiography* (ECG) or *photoplethysmography* (PPG) is neither feasible nor advisable [4]. In addition, contactless methods for VSM can be very useful in monitoring the sleep patterns of both elderly individuals and children, as well as enabling long-term in-home patient monitoring.

A relevant technical option for contactless VSM is represented by modern integrated radars operating at *millimeter-wave* (mm-wave). In fact, these devices, if placed in front of a human chest-wall are potentially able to detect its small physiological movements due to both heartbeat and respiration. Compared with traditional methods, such as ECG and PPG, radar systems make continuous and timely BR and HR monitoring possible without requiring an additional workload for nurses. Moreover, unlike light-based sensors (such as lidars and cameras), they respect the privacy of people monitored, and their measurements are not influenced by clothing [5], [6].

The technical literature on radar-based VSM has taken into consideration the use of different radar technologies; these include *continuous wave* (CW) Doppler radars [7], [8], [9], [10], [11], *impulse radio ultra-wideband* (IR-UWB) [12] and *Frequency Modulated Continuous Wave* (FMCW) radars [13], [14], [15], [16]. Continuous wave Doppler radars are characterized by a relatively simple architecture, but are unable to provide range information. Range estimation can be achieved through IR-UWB and FMCW radars. However, IR-UWB radars require a sophisticated radar architecture and circuitry, and may not guarantee a high *signal-to-noise ratio* (SNR). The FMCW technology, instead, outperforms its CW counterpart thanks to the use of frequency modulation; this results in a better SNR [17]. Moreover, recently, the technical literature on radar-based VSM has focused on

The associate editor coordinating the review of this manuscript and approving it for publication was Hasan S. Mir.

the use of colocated *multiple-input multiple-output* (MIMO) radars, i.e. of radar devices equipped with closely spaced *transmit* (TX) and *receive* (RX) antenna arrays [12], [13]. However, regardless of the employed technology, a significant challenge in the field of research on radar-based VSM remains the development of reliable and accurate signal processing methods for extracting vital sign information from radar echoes. This includes estimating specific parameters, such as average HR and BR (evaluated over a predefined observation window) and *blood pressure*, and analysing *heart rate variability* and *arrhythmias*, among others. Although recent publications are increasingly focused on proving the feasibility of detecting the subtlest vital signs, significant efforts are still required to devise signal processing methods that allow to estimate the average BR and, in particular, the average HR with an accuracy that makes them suitable for various applications. Indeed, to the best of our knowledge, the radar-based VSM devices available on the market are unable to accurately estimate both parameters. Most of the methods currently available in the technical literature are *deterministic* since their derivation is based on specific mathematical models of the electromagnetic signal reflected by a human chest; moreover, they extract vital signs through the spectral analysis of the phase of the received signal. Well known examples of this approach are represented by the *arctangent demodulator* (AD) [7] and the *cumulative phase gradient* (CPG) technique [18]. More specifically, the AD method has been originally proposed to detect cardiopulmunary activity through a quadrature Doppler radar [7]. The availability of a quadrature receiver allows to solve the so called *null point detection problem*, i.e. the dependence of detection sensitivity on target position. The AD accuracy, however, is limited by the presence of a *direct current* (DC) offset [19] as well as that of multiple high order harmonics and intermodulation products. The DC offset problem arises not only from electronic components but also from reflections off stationary objects and other parts of the human body, aside the chest wall of the monitored subject. The CPG method, instead, has been proposed for the simultaneous estimation of the BR of multiple subjects [18]. In this case, relevant information about the phase of the received signal are acquired through a *phase gradient* (PG) operation, followed by spectral analysis. More recently, the use of PG for HR and BR estimation of a single subject using a CW radar has been proposed in [20], where the *harmonic suppression phase gradient* (HSPG) algorithm is developed. Both the CPG and HSPG methods eliminate the DC offset and are able to suppress the contribution of *higher order harmonics* (HOH). However, their performance are affected by *random body movements* (RBMs) and the presence of noise in the analysed spectrum. Note also that: a) as recently shown in [18], the AD is outperformed by the CPG and HSPG methods in BR estimation and by the HSPG in HR estimation; b) as far as we know, the use of these methods for apnea detection has not been investigated yet.

In this manuscript, a novel robust and accurate radar-based method, called *Vital Signs Estimation and Apnea Detection Algorithm* (VSEADA), is proposed for VSM of a single subject. This method exploits the PG operation proposed in [18] for the extraction of relevant information from radar echoes. However, unlike [18], the VSEADA employs:

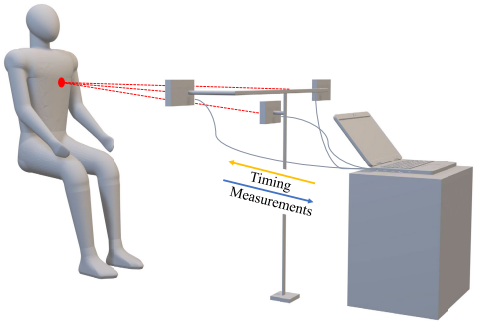

FIGURE 1. Overall architecture of the radar-based VSM system developed in our work. In this representation, three SIMO radars are mounted on a stand in front of the monitored person and are connected to the same personal computer; the last device provides the timing reference coordinating radar activity and process the acquired measurements to extract vital sign information.

1) The so-called *single frequency estimation and cancellation* (SFEC) algorithm, recently proposed in [21], for the detection and estimation of dominant spectral components.[1]

2) An innovative filtering technique, based on a Bayesian approach, for emphasizing the relevant spectral components contained in the radar signals, while suppressing the spurious ones.

3) A small network of colocated *single-input multiple-output* (SIMO) FMCW radars, synchronised in time but not in frequency and phase, to improve the quality of the acquired measurements through a selection combining mechanism.

Furthermore, in this manuscript, a *modified* CPG (MCPG) method is proposed to allow simultaneous BR and HR estimation of a single subject.

Our numerical results evidence that the VSEADA can achieve substantially better accuracy than the AD and MCPG methods, if the measurements are acquired through a couple of colocated SIMO FMCW radar devices operating at 24 GHz.

The remaining part of this manuscript is organised as follows. In Section II, the overall architecture of the proposed system is illustrated and relevant mathematical models are developed for the baseband received signal. The VSEADA is described in Section III and is compared with the AD and CPG methods in Section IV. The performance of all the considered methods is analysed in Section V. Finally, some conclusions are offered in Section VI.

Notation: Throughout this paper, $(\cdot)^*$ denotes the complex conjugate, $J_\alpha(x)$ denotes the Bessel function of the first kind of order α computed for x, $\Re\{x\}$ and $\Im\{x\}$ indicate the real and imaginary parts, respectively, of the complex variable x.

II. SYSTEM AND SIGNAL MODELS

The overall architecture of the radar-based VSM system developed in our work is illustrated in Fig. 1. This system

[1] A Matlab implementation of the SFEC is available online at [22].

consists of multiple (say, N_D) colocated SIMO FMCW radars, each equipped with N_{RX} RX antennas. These devices are assumed to be of the same type, for simplicity, and are installed on a stand, put in front of the person to be monitored; moreover, they are synchronised in time by a *personal computer* (PC), that makes them operate in a round-robin fashion (i.e., they are sequentially turned on and off, so that, at any instant, a single radar is active). Note that our architecture is related to that of the multi-radar system recently proposed in [23] to improve driver breathing estimation while reducing the overall cost with respect to a single radar equipped with a larger antenna array. The stream of measurements made available by each radar device is sent to the above-mentioned PC, on which the VSEADA is run. The remaining part of this section is devoted to describing relevant signal models; in our analysis, we refer to the SIMO radar architecture illustrated in Fig. 2. As shown

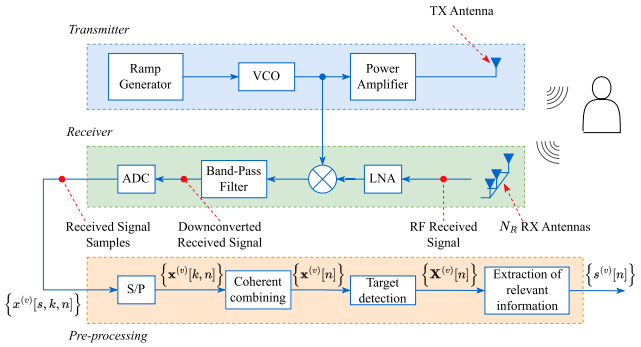

FIGURE 2. SIMO FMCW radar block diagram.

in that figure, the *radio frequency* (RF) signal radiated by the ith radar (with $i = 0, 1, \ldots, N_D - 1$) is generated by a *voltage controlled oscillator* (VCO), characterised by the free running frequency f_c (assumed to be independent of i for simplicity) and fed by a periodic ramp generator. Therefore, the transmitted signal consists of a sequence of *chirps*, each having duration

$$T_0 = T + T_R, \tag{1}$$

where T and T_R represent the *ramp time period* and the *reset time*, respectively. In the considered radar system, the transmission of chirps is organised in *frames*; more precisely, each frame is composed by N_C consecutive chirps (called *Doppler* chirps, since, as shown below, they are jointly processed for Doppler estimation) and its duration is

$$T_F = N_C T_0 + T_I, \tag{2}$$

where T_I, called *idle time*, is the duration of the time interval separating each couple of consecutive frames. The time evolution of the instantaneous frequency of the radiated signal is shown in Fig. 3, where $N_C = 3$ is assumed. It is important to point out that, in the considered radar system, T_I is much greater than T_0. This allows us to allocate one transmission and reception of each radar device in the idle time of the remaining $(N_D - 1)$ devices, so that mutual interference is avoided. All the chirps transmitted (and received) by the N_D devices during the time interval between the beginning of the transmission of the first chirp within a frame related to the dth radar device ($d \in \{0, 1, .., N_D - 1\}$), and the beginning of the first chirp in the subsequent frame of the same radar device, are said to belong to the same *superframe*. A simple example of the time evolution of the instantaneous frequency of the signals radiated during a superframe is shown in Fig. 4, that refers to the case in which $N_D = 2$. Note that, in general, the duration of each superframe, denoted T_{SF}, is equal to the duration of the frame T_F. In the following, the term frame will be used when discussing an individual radar device. Conversely, when dealing with multiple radars, we will employ the term superframe.

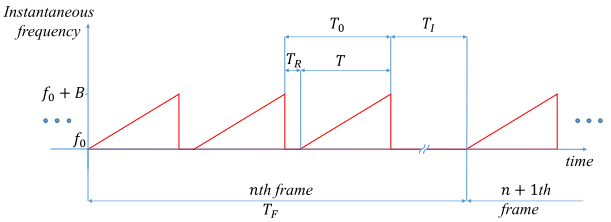

FIGURE 3. Representation of the time evolution of the instantaneous frequency characteristic each of employed SIMO FMCW radars; $N_C = 3$ is assumed.

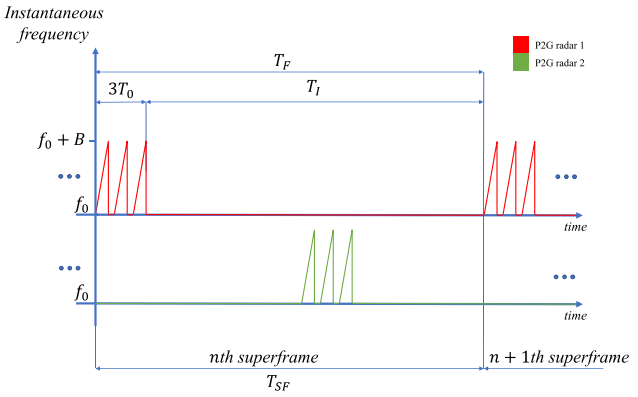

FIGURE 4. Representation of the time evolution of the instantaneous frequency of the signals radiated during a superframe. The use oftwo distinct radar devices (i.e., $N_D = 2$) is assumed.

The electromagnetic signal radiated by each radar is reflected by the chest of the monitored person. The derivation of a mathematical model for the radar echo requires the knowledge of the time evolution of the *chest displacement*, i.e. of the time-varying distance between the radar and the chest itself. The chest displacement is composed of [13] and [18]: a) relatively large movements due to the *inspiration and expiration phases*; b) small oscillations due to heart activity; c) RBMs having unpredictable amplitude. If RBMs are ignored and a *point target model* is adopted for the human chest, the chest displacement at the instant t can be expressed as [8]

$$\Delta R(t) \triangleq R(t) - R_0 = \delta_b(t) + \delta_h(t), \tag{3}$$

where $\delta_b(t)$ ($\delta_h(t)$) denote the breath (heart) contributions to $\Delta R(t)$ and $R(t)$ (R_0) represent the radar-chest distance at time t (distance measured in the absence of any activity[2]). Accurate models for $\delta_b(t)$ and $\delta_h(t)$ have been proposed in [24]. However, in our work, the *simplified point target model* (SPTM) illustrated in [25], [26], and [27] is adopted. For this reason, it is assumed that

$$\delta_b(t) = \frac{\delta_{b,M}}{2}\left[1 - \cos(\omega_b t)\right], \tag{4}$$

for both the inspiration and expiration phases of the breathing period and

$$\delta_h(t) = \delta_{h,M}\cos(\omega_h t), \tag{5}$$

for the heart displacement, where $\omega_b \triangleq 2\pi f_b = 2\pi/T_b$, $\omega_h \triangleq 2\pi f_h = 2\pi/T_h$; here, f_b (T_b) and f_h (T_h) are the BR (breath period) and HR (heart period), respectively, and $\delta_{b,M}$ and $\delta_{h,M}$ represent the maximum absolute values of breath displacement and heart displacement, respectively. It is worth mentioning that: a) typical values of $\delta_{b,M}$ range from 8 to 24 mm, whereas those of $\delta_{h,M}$ range from 0.4 to 0.5 mm [12]; b) the breath (heart) rate usually ranges from $f_{b,min} = 0.1$ Hz ($f_{h,min} = 0.883$ Hz) to $f_{b,max} = 0.5$ Hz ($f_{h,max} = 2.667$ Hz) [13], [18], [28].

In the remaining part of this section we focus on a single SIMO radar device (namely, on the active one) and, to simplify the adopted notation, we omit the dependence of the considered mathematical models on the radar index (i.e., on d). The meaning of the most relevant parameters, sets, vectors and matrices of the VSEADA and its pre-processing stage (see Section III) is summarized[3] in Table 1. As shown in Fig. 2, at the RX side of this device, the electromagnetic echo originating from the chest of the monitored person is captured by the N_{RX} antennas forming the RX array. Consequently, the N_{RX} received signals undergo amplification, quadrature downconversion and analog-to-digital conversion; these three tasks are accomplished by a *low noise amplifier* (LNA) and, for both the in-phase and quadrature components, by a mixer & band-pass filter and an *analog-to-digital converter* (ADC), respectively. The resulting sample stream feeds a *pre-processing* stage, on which we focus in the remaining part of this section. To simplify our mathematical developments, we make the following assumptions about the range model (3): a) the displacement $\Delta R(t)$ is always much smaller than R_0 (in practice, the chest displacement is in the order of a few millimeters, whereas the chest-radar distance is in the order of one meter); b) in the absence of RBMs, the displacement $\Delta R(t)$ undergoes minimal changes within each frame, as the frame period T_F is significantly shorter than the heart period T_h (in particular, T_F and T_h are not greater than 0.1 s and 0.4 s, respectively). Consequently, the variations observed in the frequency of the downconverted received signals within each frame, as well as those from antenna to antenna within a given frame, and the phase variations of the same signals within each chirp, can be deemed negligible. Based on all this, the kth complex sample acquired through the vth RX antenna during the sth chirp interval of the nth frame[4] can be approximated as [29]

$$x^{(v)}[k,s,n] \simeq a^{(v)}[s]\exp(j(2\pi k f_n T_s + \psi^{(v)}[s,n])) + w^{(v)}[k,s,n] \tag{6}$$

with $v = 0, 1, .., N_{RX} - 1$, $k = 0, 1, \ldots, N-1$ and $s = 0, 1, \ldots, N_C - 1$; here, T_s is the sampling interval, N is the overall number of samples acquired over a single chirp interval, $w^{(v)}[k,s,n]$ is the complex Gaussian noise sample affecting $x^{(v)}[k,s,n]$, and $a^{(v)}[s]$, f_n and $\psi^{(v)}[s,n]$ denote the amplitude, frequency and phase, respectively, of the useful component of $x^{(v)}[k,s,n]$. It can be shown that [13], [14], [30]

$$f_n = 2\mu\frac{R_0}{c} \tag{7}$$

and

$$\psi^{(v)}[s,n] = \frac{4\pi}{\lambda}R^{(v)}[s,n] \tag{8}$$

where $\mu = B/T$ is the chirp slope, B is the width of the swept frequency interval (i.e., the radar bandwidth), $\lambda = f_c/c$ is the radar wavelength and $R^{(v)}[n]$ is the distance of vth RX antenna from the chest of the monitored subject during the nth frame interval. Based on the model (3), (8) can be rewritten as

$$\psi^{(v)}[s,n] = \psi_0 + \Delta\psi^{(v)}[s,n], \tag{9}$$

where

$$\psi_0 = 4\pi\frac{R_0}{\lambda} \tag{10}$$

is a constant phase shift depending on the distance R_0 and

$$\Delta\psi^{(v)}[s,n] = \frac{4\pi}{\lambda}\Delta R^{(v)}[s,n] \tag{11}$$

represents the phase shift due to the range variation $\Delta R^{(v)}[s,n]$.

In the considered radar system, vital sign estimation is based on the measurements acquired over N_F frames; in the following, we focus, for the considered radar device, on the frames associated with $n = 0, 1, \ldots, N_F - 1$ and describe the processing executed on the set $\{x^{(v)}[k,s,n]\}$, that collects $N_{RX}N_C N$ complex measurements acquired over those frames. Such a processing evolves through the three steps described below for the vth RX antenna.

1) *Coherent combining* - The measurements acquired in N_C chirp intervals of the nth frame are *coherently combined* for SNR enhancement. This task relies on the assumption that the chirp duration is much smaller than the minimum heart period

[2]Note that, in general, this distance changes from radar to radar in the system represented in Fig. 1.

[3]For the sake of simplicity, only the parameters, set and vectors adopted in our description of HR estimation are listed in Table 1; the notation employed for their counterparts in BR estimation is straightforward.

[4]In the literature, k and n are called *fast time* index and *slow time* index, respectively [4].

TABLE 1. Most relevant parameters, sets, vectors and matrices appearing in our description of the VSEADA and the associated pre-processing stage.

No.	Parameter	Description
1	$x^{(v)}[k,s,n]$	kth complex sample available at the ADC ouput and acquired through the vth antenna during the sth chirp interval of the nth frame
2	$\psi^{(v)}[s,n]$	Phase of the useful component of $x^{(v)}[k,s,n]$
3	$\Delta\psi^{(v)}[s,n]$	Phase shift due to the range variation $\Delta R^{(v)}[s,n]$
4	$x^{(v)}[k,n]$	Coherent combination of $\{x^{(v)}[k,s,n]; s=0,1,...,N_{\rm C}-1\}$
5	$\mathbf{X}^{(v)}$	Matrix collecting the DFT coefficients of the sequence $\{x^{(v)}[k,n]; k=0,1,...,N-1\}$
6	$\hat{l}^{(v)}[n]$	Estimate of the the frequency bin index associated with the strongest target for the vth antenna and the nth frame
7	$s^{(v)}[n]$	Relevant spectral information extracted from $\mathbf{X}^{(v)}$ for $l=\hat{l}^{(v)}[n]$
8	$\{l_{\min}, l_{\max}\}$	Minimum and maximum bin indices, associated with $R_{\min}$ and $R_{\max}$, and employed to limit the region for target search
8	$\mathbf{s}_p^{(v)}$	Vector collecting the pre-processed measurements of the pth data block for the vth antenna
9	$\mathbf{g}_{0,p}^{(v)}$	Vector collecting the phase gradient elements computed for $\mathbf{s}_p^{(v)}$
10	$\mathbf{F}_{\rm x}^{(v)}[p]$	Vector collecting the normalized frequencies of the $M_{\rm x}$ strongest tones of $\mathbf{g}_{0,p}^{(v)}$ estimated by the SFEC algorithm
11	$\mathbf{A}_{\rm x}^{(v)}[p]$	Vector collecting the complex amplitudes of the $M_{\rm x}$ strongest tones of $\mathbf{g}_{0,p}^{(v)}$ estimated by the SFEC algorithm
12	$\mathbf{a}_{\rm x}^{(v)}[p]$	Vector collecting the absolute values of the complex amplitudes $\mathbf{A}_{\rm x}^{(v)}[p]$
13	$Q^{(v)}[p]$	Quality index computed for the vth antenna in the pth data block
14	$\bar{\mathcal{S}}_{\rm h}[p]$	Set collecting the spectral information available after antenna selection for the pth data block
15	$\xi[p]$	Binary value indicating the presence of an apnea event in the pth data block
16	$\mathcal{A}_{\rm h}$	Set collecting the possible values taken by the discrete state variable representing the HR
17	$\hat{\alpha}_m^{(\rm h)}[p]$	Probability that the HR belongs to the mth bin in the pth data block
18	$\Delta_m^{(\rm h)}$	Set collecting the indices of the bins of the $(p-1)$th data block from which the mth bin can be reached in the pth data block
19	$\{\hat{n}_{\min}^{(\rm h)}[m], \hat{n}_{\max}^{(\rm h)}[m]\}$	Minimum and maximum bin indices of the bins in the $(p-1)$th data block from which the mth bin in the pth data block can be reached
20	$\beta_{m\|l}^{(\rm h)}$	State transition probability associated with the transition from the mth bin to the lth bin.
21	$\gamma_n^{(\rm h)}[p]$	Probability that the HR falls in the nth frequency bin based on the SFEC algorithm output available for the pth data block
22	$\alpha_n^{(\rm h)}[p]$	Probability that the HR belongs to the nth frequency bin during the $(p-1)$th data block
23	$\bar{\mathbf{a}}_{\rm h}[p]$	Vector collecting the amplitudes estimated by the SFEC algorithm for the pth data block and the repetition of the same values
24	$\bar{\mathbf{F}}_{\rm h}[p]$	Vector collecting the normalised frequencies estimated by the SFEC algorithm for the pth data block and a repetition of the same values divided by two
25	$\mu_i^{(\rm h)}[p]$	Mean of the ith component of the probability density function $f_p^{(\rm h)}(x)$
26	$(\sigma_i^{(\rm h)}[p])^2$	Variance of the ith component of the probability density function $f_p^{(\rm h)}(x)$
27	$\hat{n}^{(\rm h)}[p]$	Index of the most likely state (frequency bin) after the measurement update based on the pth data block
28	$\hat{f}_{\rm h}[p]$	HR estimate evaluated on the basis of $\hat{n}^{(\rm h)}[p]$
29	$\alpha_n^{(\rm h)}[-1]$	Initial value of $\alpha_n^{(\rm h)}[p]$ selected for the filtering algorithm

(i.e., that $T_0 \ll T_{\rm h,min}$, with $T_{\rm h,min} = 1/f_{\rm h,max} = 0.37$s), so that the approximation

$$\psi^{(v)}[s,n] \cong \psi^{(v)}[n] \tag{12}$$

holds for $s \in \{0,1,\ldots,N_{\rm C}-1\}$. Moreover, it is accomplished by evaluating

$$x^{(v)}[k,n] = \sum_{s=0}^{N_{\rm C}-1} x^{(v)}[k,s,n] \tag{13}$$

for $k = 0,1,\ldots,N-1$ and $n = 0,1,\ldots,N_{\rm F}-1$; this produces the new set $\{x^{(v)}[k,n]\}$, consisting of $NN_{\rm F}$ complex measurements. A simple model for $x^{(v)}[k,n]$ can be derived substituting the *right hand side* (RHS) of (6) in that of (13) and taking into account the approximation (12); this yields

$$x^{(v)}[k,n] = b^{(v)} \exp(j(2\pi k f_{\rm n} T_{\rm s} + \psi^{(v)}[n])) + w_{\rm s}^{(v)}[k,n], \tag{14}$$

where

$$b^{(v)} = \sum_{s=0}^{N_{\rm C}-1} a^{(v)}[s] \tag{15}$$

and

$$w_{\rm s}^{(v)}[k,n] = \sum_{s=0}^{N_{\rm C}-1} w^{(v)}[k,s,n]. \tag{16}$$

2) *Target detection* - For each frame (i.e., for each n), the sequence $\{x^{(v)}[k,n]\}$, consisting of N elements, undergoes zero padding followed by order N_0 *discrete Fourier transform* (DFT) processing; here, $N_0 = M \cdot N$, where M denotes the selected oversampling factor. This produces the $N_0 \times N_{\rm F}$ complex matrix

$$\mathbf{X}^{(v)} \triangleq [X^{(v)}[l,n]], \tag{17}$$

where

$$X^{(v)}[l,n] = \frac{1}{N_0} \sum_{k=0}^{N-1} x_{\rm zp}^{(v)}[k,n] \exp(-j2\pi kl/N_0), \tag{18}$$

with $l = 0, 1, \ldots, N_0 - 1$ and $n = 0, 1, \ldots, N_F - 1$; here, $\{x_{zp}^{(v)}[k, n]\}$ is the zero padded version of $\{x^{(v)}[k, n]\}$, for any n. Then, the index of the frequency (i.e., range) bin[5] associated with the target (i.e., the chest of the monitored person) is evaluated as

$$\hat{l}^{(v)}[n] = \arg \max_{\tilde{l} \in \{l_{min}, \ldots, l_{max}\}} |X^{(v)}[\tilde{l}, n]|, \tag{19}$$

where the limits l_{min} and l_{max} on the search interval are selected on the basis of our prior knowledge about the chest distance from the radar.

3) *Extraction of relevant spectral information* - Given $\hat{l}^{(v)}[n]$ (19), relevant spectral information is extracted from the matrix $\mathbf{X}^{(v)}$ (17) by computing the quantity

$$s^{(v)}[n] \triangleq X^{(v)}[\hat{l}^{(v)}[n], n] \tag{20}$$

for $n = 0, 1, \ldots, N_F - 1$. This concludes the pre-processing steps.

The N_{RX} sequences $\{s^{(v)}[n]; n = 0, 1, \ldots, N_F - 1\}$ feed the VSEADA. The processing accomplished by this algorithm is based on the assumption that, for any v, the measurement $s^{(v)}[n]$ can be modelled as (the derivation of the following result is sketched in Appendix A)

$$s^{(v)}[n] = b^{(v)} \exp(j\psi^{(v)}[n]) + w_R^{(v)}[n] \tag{21}$$

for $n = 0, 1, \ldots, N_F - 1$; here, $b^{(v)}$ represents the amplitude of the chest echo (depending on its position and reflectivity), $w_R^{(v)}[n]$ is the noise affecting the considered measurement and (see (9)-(11), and the approximation (12))

$$\psi^{(v)}[n] = \frac{4\pi}{\lambda}(R_0 + \Delta R^{(v)}[n]). \tag{22}$$

Our description of the proposed radar system and of the adopted models deserves various comments that are listed below.

Multipath mitigation in VSM - The pointwise model illustrated above is commonly adopted in the technical literature on radar-based VSM. Unluckily, this model does not account for the fact that: a) the received signal is actually the superposition of multiple echoes, originating not only from the body of the monitored subject, but also from any target detectable in the considered propagation environment (usually, an indoor environment); b) the human chest, being quite close to the radar device (its typical distance is in the order of 1-2 meters) behaves like an *extended target* and, consequently, generates multiple echoes that may interfere in a constructive or destructive fashion at each of the RX antennas. For these reasons, the communication channel characterizing the employed radar system is affected by *multipath fading*; this phenomenon can completely disrupt the (weak) breath and heart signatures in radar-based VSM. These considerations have allowed us to interpret our experimental results; in fact, such results have evidenced that:

[5]Note that the use of an order N_0 DFT in (18) leads to partitioning the frequency interval of interest in N_0 distinct frequency (i.e., range) *bins*.

a) The quality of the signals acquired through different RX antennas of a given radar device in the same observation interval can be substantially different [31]. In particular, as shown in Section V, a portion of such signals is useless, since their amplitude spectra do not exhibit significant peaks; in fact, this entails that the expected breath and heart signatures cannot be easily identified.

b) The quality of the signal provided by a given RX antenna is time varying. In other words, an RX antenna providing relevant spectral information in a certain observation interval can become useless in a different interval.

The impact of multipath fading can be mitigated by exploiting the *spatial diversity* provided by a single radar equipped with a reasonably large array; in this case, *beamforming* techniques could be employed [15], [32], [33]. In our work, we opted for a different strategy, which is simpler from a signal processing perspective and lends itself to a more cost-effective implementation. In fact, we decided to take advantage of the diversity offered by multiple (say, N_D) radars. This solution was originally proposed by Rong et al. [34] to compensate body motions in VSM through a couple of IR-UWB radars. In [35], the same system has been employed for VSM of a single subject performing large movements, while, in [36], two IR-UWB radars with distinct centre frequencies have been employed for the estimation of vital signs from multiple subjects. In our work, the N_D FMCW radars are equipped with small RX arrays and adopt a *selection combining* strategy. For this reason, as shown in the next section, in each superframe, the VSEADA selects, among the set of $\tilde{N}_{RX} \triangleq N_{RX}N_D$ sequences $\{s^{(v)}[n]; n = 0, 1, \ldots, N_F - 1\}$, the $\bar{N}_{RX}$ sequences offering the spectrally richest information for vital sign detection.

Exploitation of prior information about the position of the monitored person - If the only target in the radar *field-of-view* (FOV) was the patient's chest, $l_{min} = 0$ and $l_{max} = N_0 - 1$ could be selected in (19). Unfortunately, in a real-world scenario, the presence of multiple targets can result in several spectral peaks, some of which can be stronger than the one associated with the patient's chest. When this happens, (19) leads to selecting the wrong spectral bin; when this occurs, vital sign information is lost. This is exemplified by Fig. 5, in which the range profile from a single antenna and for $N_F = 317$ frames is shown; here, the yellow portions of the plot refer to the strongest targets located within the radar FOV. In this scenario, the range bin at 5.5 m (corresponding to the wall position) would be erroneously selected as the patient's chest, which is instead located at approximately 1 m and is represented by the black horizontal line in the figure. If the range of the patient's chest is known to belong to the interval $[R_{min}, R_{max}]$, l_{min} and l_{max} can be evaluated as (see (7))

$$l_{min} = \left\lfloor \frac{2\mu N_0 T_s R_{min}}{c} \right\rfloor \tag{23}$$

and

$$l_{max} = \left\lceil \frac{2\mu N_0 T_s R_{max}}{c} \right\rceil, \tag{24}$$

respectively. In Fig. 5, the introduction of range limitations at $R_{\min} = 0.5$ m and $R_{\max} = 1.5$ m, represented by red horizontal lines, allows one to properly select the patient's chest through (19).

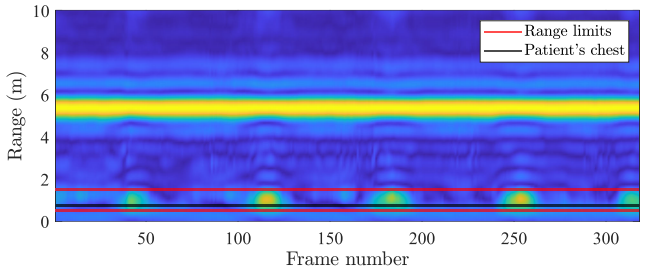

FIGURE 5. Representation of a range profile for $N_F = 317$ frames and from a single RX antenna. The range limits, represented as red horizontal lines, are set to avoid the wall (recognisable as the strongest target at 5.5 m) from being selected by (19) as the patient's chest. The latter is represented by a black horizontal line and is located at approximately 1 m.

Data processing - As a matter of fact, HR and BR are time-varying parameters and, in VSM, their fluctuations need to be carefully tracked; in doing so, the existing correlation between the values observed for these parameters in adjacent time intervals should be exploited. In the VSEADA, the following approach is adopted. The stream of superframes provided by the N_D radar devices is divided into partially overlapped blocks (called *data blocks*), each consisting of N_B consecutive superframes (and, consequently, lasting $N_B T_{SF}$ s), as shown in Fig. 6; note that the beginning of each data block is shifted by N_s superframe intervals with respect to the beginning of the previous one, with $N_s < N_B$. New estimates of HR and BR are evaluated over each data block and, consequently, are made available every $N_s T_{SF}$ s; however, as shown in the following section, they are processed by a filtering algorithm to exploit the above-mentioned correlation. It is important to keep in mind that the duration of each data block must be selected in such a way that sufficiently accurate estimates of BR[6] are obtained. Our experiments have evidenced that the duration of each data block should cover at least two consecutive periods of respiration; this means that N_B should be selected in a way that the inequality $N_B T_{SF} > 2T_{b,\min}$ holds.

III. DESCRIPTION OF THE VITAL SIGNS ESTIMATION AND APNEA DETECTION ALGORITHM

The inner structure of the VSEADA is described by the block diagram shown in Fig. 7. In this section, the signal processing tasks accomplished by the blocks appearing in this diagram are analysed. In our description, we show how the pth data block is processed to estimate both HR and BR, and how the estimates extracted from consecutive data blocks are filtered to improve the overall accuracy.

1) *Computation of the phase gradient* - The first block of Fig. 7 is fed by the set $\{\mathbf{s}_p^{(v)}; v = 0, 1, \ldots, \tilde{N}_{RX} - 1\}$, that

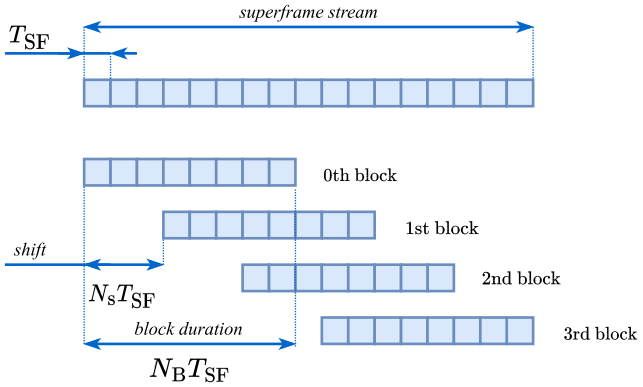

FIGURE 6. Representation of data block generation. In this case, four partially overlapped blocks, each collecting the measurements acquired over $N_B = 8$ consecutive superframes, are extracted from the available sequence of superframes and the block shift N_s is equal to 3.

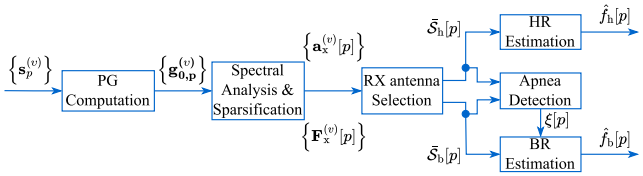

FIGURE 7. Architecture of the VSEADA.

collects all the measurements forming the pth data block, where

$$\mathbf{s}_p^{(v)} \triangleq \left[s_p^{(v)}[0], s_p^{(v)}[1], \ldots, s_p^{(v)}[N_B - 1]\right]^T \quad (25)$$

represents the contribution of the vth RX antenna; here,

$$s_p^{(v)}[n] \triangleq s^{(v)}[pN_s + n]. \quad (26)$$

For any v, the $(N_B - \Delta n)$-dimensional vector

$$\mathbf{g}_{0,p}^{(v)} \triangleq \left[g_{0,p}^{(v)}[0], g_{0,p}^{(v)}[1], \ldots, g_{0,p}^{(v)}[N_B - \Delta n - 1]\right]^T, \quad (27)$$

conveying information about the phase variations (i.e., about the PG) observed over consecutive samples of the sequence $\{s_p^{(v)}[n]\}$, is evaluated. The nth element of the vector $\mathbf{g}_{0,p}^{(v)}$ (27) is evaluated as

$$g_{0,p}^{(v)}[n] \triangleq \Im\left\{f_{0,p}^{(v)}[n]\right\}, \quad (28)$$

where

$$f_{0,p}^{(v)}[n] \triangleq s_p^{(v)}[n] \cdot \left(s_p^{(v)}[n + \Delta n]\right)^* \quad (29)$$

is the nth element of the so-called PG sequence [18]; here, Δn is a positive integer parameter,[7] called *time lag*.

2) *Spectral analysis and sparsification* - In the second block of Fig. 7, the spectral content of each of the $\tilde{N}_{RX}$ vectors $\{\mathbf{g}_{0,p}^{(v)}\}$ (27) is analysed and a sparse representation of it is generated. These tasks are accomplished by the SFEC algorithm illustrated in [37, Par. III.B]. This algorithm detects, for any v, the dominant sinusoidal components of the sequence $\{g_{0,p}^{(v)}[n]\}$ and estimates their parameters

[6]Note that respiration, being a phenomenon slower than heartbeat, requires a longer observation interval for its estimation.

[7]A small value is selected for this parameter in order to avoid the *phase wrapping* phenomenon.

(namely, their normalised frequency and complex amplitude). In practice, for any v, the vector $\mathbf{g}_{0,p}^{(v)}$ is employed to generate the $(N_{\mathrm{B}} - \Delta n)$-dimensional vector

$$\mathbf{g}_{q,p}^{(v)} \triangleq \left[g_{q,p}^{(v)}[0], g_{q,p}^{(v)}[1], \ldots, g_{q,p}^{(v)}[N_{\mathrm{B}} - \Delta n - 1] \right]^T, \quad (30)$$

where

$$g_{q,p}^{(v)}[n] \triangleq n^q g_{0,p}^{(v)}[n] \quad (31)$$

with $n = 0, 1, \ldots, N_{\mathrm{B}} - \Delta n - 1$, and $q = 1$ and 2. Then, for any v, the vectors $\{\mathbf{g}_{0,p}^{(v)}, \mathbf{g}_{1,p}^{(v)}, \mathbf{g}_{2,p}^{(v)}\}$ undergo zero-padding followed by order N_0' DFT processing; here, $N_0' = M'(N_{\mathrm{B}} - \Delta n)$ and M' represent the selected oversampling factor. This produces the N_0'-dimensional vector

$$\mathbf{G}_q^{(v)} \triangleq \left[G_q^{(v)}[0], G_q^{(v)}[1], \ldots, G_q^{(v)}[N_0' - 1] \right]^T, \quad (32)$$

with $v = 0, 1, \ldots, \tilde{N}_{\mathrm{RX}} - 1$ and $q = 0, 1, 2$; here,

$$G_q^{(v)}[l] = \frac{1}{N_0'} \sum_{n=0}^{N_{\mathrm{B}} - \Delta n - 1} g_{q,p}^{(v)}[n] \exp(-j2\pi nl/N_0'), \quad (33)$$

with $l = 0, 1, \ldots, N_0' - 1$. Then, for any v, the set $\{\mathbf{G}_q^{(v)}; q = 0, 1, 2\}$, collecting three different spectra, is processed by an algorithm that, in each of its iterations, detects the dominant tone, estimates its parameters, and cancels its contribution to those spectra. In this case, our prior knowledge about the typical frequency ranges of HR and BR is exploited. For this reason, the SFEC algorithm is executed twice. More specifically, in its first execution, it is employed to detect the M_{b} strongest tones falling in the frequency range of *breath* and estimates their parameters. In doing so, tone detection, which is based on the well-known *periodogram method* (e.g., see [38]), is restricted to the frequency range $[f_{\mathrm{b,min}}, f_{\mathrm{b,max}}]$, encompassing typical BRs. The second execution of the SFEC algorithm, instead, aims at detecting and estimating the M_{h} strongest tones in a different frequency range and, in particular, in the range $[f_{\mathrm{h,min}}, 2f_{\mathrm{h,max}}]$, that contains both the *first harmonic* (FH) and the *second harmonic* (SH) of heart activity. The last choice is motivated by the fact that, as evidenced by our experimental results (see Section V), the heart SH may be significantly stronger than the associated FH; this phenomenon is unpredictable and clearly evidences the limitations of the model adopted for the representation of chest displacement (see (3)-(5)).

The SFEC outputs are the two M_{x}-dimensional vectors (see [21, Sec. III.B])

$$\mathbf{F}_{\mathrm{x}}^{(v)}[p] = \left[F_{\mathrm{x},0}^{(v)}[p], F_{\mathrm{x},1}^{(v)}[p], \ldots, F_{\mathrm{x},M_{\mathrm{x}}-1}^{(v)}[p] \right] \quad (34)$$

and

$$\mathbf{A}_{\mathrm{x}}^{(v)}[p] = \left[A_{\mathrm{x},0}^{(v)}[p], A_{\mathrm{x},1}^{(v)}[p], \ldots, A_{\mathrm{x},M_{\mathrm{x}}-1}^{(v)}[p] \right], \quad (35)$$

collecting the normalised frequencies[8] and the associated complex amplitudes, respectively, of the M_{x} strongest tones potentially related to breath (if x = b) and heart (if x = h) activities and detected on the vth RX antenna (with $v = 0, 1, \ldots, \tilde{N}_{\mathrm{RX}} - 1$). Then, for any v, the vector

$$\mathbf{a}_{\mathrm{x}}^{(v)}[p] = \left[a_{\mathrm{x},0}^{(v)}[p], a_{\mathrm{x},1}^{(v)}[p], \ldots, a_{\mathrm{x},M_{\mathrm{x}}-1}^{(v)}[p] \right], \quad (36)$$

made of the amplitudes of the same tones, is generated for x = b and h; here, $a_{\mathrm{x},m}^{(v)}[p] \triangleq |A_{\mathrm{x},m}^{(v)}[p]|$ for $m = 0, 1, \ldots, M_{\mathrm{x}} - 1$.

Note that the sets $\{\mathbf{F}_{\mathrm{x}}^{(v)}[p]; v = 0, 1, \ldots, \tilde{N}_{\mathrm{RX}} - 1\}$ and $\{\mathbf{a}_{\mathrm{x}}^{(v)}[p]; v = 0, 1, \ldots, \tilde{N}_{\mathrm{RX}} - 1\}$ provide, for the vth RX antenna, a *sparse representation* of the spectral content potentially originating from breath (if x = b) and heart (if x = h) activities during the pth data block.

3) *Antenna selection* - In the *third block* of Fig. 7, the quality of the spectral information provided by the vth RX antenna is assessed on the basis of the vector $\mathbf{a}_{\mathrm{x}}^{(v)}[p]$ (36) (with $v = 0, 1, \ldots, \tilde{N}_{\mathrm{RX}} - 1$). Then, only the best RX antennas are selected for further processing. More precisely, our antenna selection strategy consists of: a) evaluating the *quality index*

$$Q^{(v)}[p] \triangleq \sum_{l=0}^{M_{\mathrm{h}}-1} (a_{\mathrm{h},l}^{(v)}[p])^2 + \sum_{l=0}^{M_{\mathrm{b}}-1} (a_{\mathrm{b},l}^{(v)}[p])^2, \quad (37)$$

for the vth antenna (with $v = 0, 1, \ldots, \tilde{N}_{\mathrm{RX}} - 1$); b) selecting the antennas associated with the $\bar{N}_{\mathrm{RX}}$ largest values of it. Note that $Q^{(v)}[p]$ (37) is proportional to the overall energy associated with the $(M_{\mathrm{b}} + M_{\mathrm{h}})$ tones that have been detected by the SFEC algorithm and that the choice of this index is motivated by our experimental results. In fact, our measurements have evidenced that spectra of poor quality (i.e., those in which spectral peaks related to heart and respiration activities cannot be easily identified [39]) are usually associated with low values of the adopted index. Further details on this are provided in Sec. V-B

The spectral information available after antenna selection for the pth data block is collected in the sets

$$\bar{\mathcal{S}}_{\mathrm{h}}[p] = \left\{ \left(\mathbf{F}_{\mathrm{h}}^{(v)}[p], \mathbf{a}_{\mathrm{h}}^{(v)}[p] \right); v = v_0, v_1, \ldots, v_{\bar{N}_{\mathrm{RX}}-1} \right\} \quad (38)$$

and

$$\bar{\mathcal{S}}_{\mathrm{b}}[p] = \left\{ \left(\mathbf{F}_{\mathrm{b}}^{(v)}[p], \mathbf{a}_{\mathrm{b}}^{(v)}[p] \right); v = v_0, v_1, \ldots, v_{\bar{N}_{\mathrm{RX}}-1} \right\} \quad (39)$$

referring to heart and respiration, respectively; here, v_k denotes the index of the kth selected antenna. The set $\bar{\mathcal{S}}_{\mathrm{h}}[p]$ (38) is processed for HR estimation and with the set $\bar{\mathcal{S}}_{\mathrm{b}}[p]$ for apnea detection. For BR estimation, instead, only the set $\bar{\mathcal{S}}_{\mathrm{b}}[p]$ (39) is employed. These tasks are executed in the remaining three blocks of Fig. 7.

4) *Apnea detection* - The sets $\bar{\mathcal{S}}_{\mathrm{h}}[p]$ (38) and $\bar{\mathcal{S}}_{\mathrm{b}}[p]$ (39) are passed to the *fourth block* of Fig. 7. This block is used to detect apnea events, which are characterised by the disappearance of the breath peak in the spectral region of interest. The output is a binary variable, denoted $\xi[p]$, whose value is set to 1 (0) if an apnea event is detected (not detected) in the pth data block. The strategy adopted in our work for the

[8]The normalised frequency F associated with the frequency f is defined as $F \triangleq fT_{\mathrm{SF}}/N_0'$, where T_{SF} and N_0' represent the superframe period and the DFT order adopted by the SFEC algorithm, respectively.

generation of $\xi[p]$ can be expressed as

$$\xi[p] \triangleq \begin{cases} 1 & \text{if } a_{\mathrm{h,max}}[p] > a_{\mathrm{b,max}}[p] \\ 0 & \text{everywhere else} \end{cases} \tag{40}$$

where $a_{\mathrm{h,max}}[p]$ and $a_{\mathrm{b,max}}[p]$ represent the largest elements of all the vectors of the sets $\{\mathbf{a}_{\mathrm{h}}^{(v)}[p];\, v = v_0, v_1, \ldots, v_{\bar{N}_{\mathrm{RX}}-1}\}$ and $\{\mathbf{a}_{\mathrm{b}}^{(v)}[p];\, v = v_0, v_1, \ldots, v_{\bar{N}_{\mathrm{RX}}-1}\}$, respectively.

5) *Heart rate estimation* - The set $\bar{\mathcal{S}}_{\mathrm{h}}[p]$ (38) feeds the *fifth* block of Fig. 7. The task accomplished by this block is the estimation of HR. In developing an algorithm for achieving this result, the following specific issues, emerging from the spectral analysis of our measurements, were taken into account:

a) The heart harmonics are usually much weaker than the harmonics due to respiration. Moreover, the strongest spectral peak observed in the typical range of heart frequencies does not necessarily correspond to the heart signature, but may originate from multipath or noise contributions.

b) The amplitude of the heart SH can be significantly stronger than that of the associated FH. This phenomenon has been observed for the first time by Park et al. [40] and motivates our attempt to exploit both spectral contributions to achieve a reliable HR estimate.

c) The intensities of the heart FH and SH are random and time-varying.

These issues make the problem of HR estimation really hard to solve. The solution we developed exploits the correlation of the HR observed over consecutive data blocks and is based on a *Bayesian filtering* approach (e.g., see [41]). In fact, our estimation method consists of two steps, namely a *time update* followed by a *measurement update*. It is important to point out that, in principle, the derivation of the algorithm to be executed in the time update and measurement update would require the knowledge of the statistical models describing the time evolution of HR (i.e., the *state model*) and relating the HR to radar measurements (i.e., the *measurement model*), respectively. In our work, since both models were unavailable, the following heuristic approach has been adopted. First, the HR over each data block has been represented as a *discrete state variable*,[9] that can take on N_{h} distinct integer values. More specifically, it has been assumed that the values of this state variable belong to the set

$$\mathcal{A}_{\mathrm{h}} = \{n_{\mathrm{min}}^{(\mathrm{h})}, n_{\mathrm{min}}^{(\mathrm{h})} + 1, \ldots, n_{\mathrm{min}}^{(\mathrm{h})} + N_{\mathrm{h}} - 1\}; \tag{41}$$

the elements of this set represent the indices of the N_{h} frequency bins resulting from the order N_0' DFT processing (see (33) with $q = 0$) and falling in the frequency range $[f_{\mathrm{h,min}}, 2f_{\mathrm{h,max}}]$. Then, we have devised a simple algorithm for updating the probability that the HR takes on a specific value of $\mathcal{A}_{\mathrm{h}}$ (i.e., falls inside a specific frequency bin) over a given data block; this algorithm, that represents the *time update* of our filtering method, can be summarised as follows. Let $\alpha_n^{(\mathrm{h})}[p-1]$ denote the probability that the HR belongs to the nth frequency bin during the $(p-1)$th data block, with $n \in \mathcal{A}_{\mathrm{h}}$; then, the prediction $\hat{\alpha}_m[p]$ of the probability that the HR will fall inside the mth bin in the next (i.e., in the pth) data block can be evaluated as

$$\hat{\alpha}_m^{(\mathrm{h})}[p] = \sum_{l \in \Delta_m^{(\mathrm{h})}} \alpha_l^{(\mathrm{h})}[p-1]\, \beta_{m|l}^{(\mathrm{h})}, \tag{42}$$

with $m \in \mathcal{A}_{\mathrm{h}}$ (see (41)); here, $\beta_{m|l}^{(\mathrm{h})}$ denotes the probability of observing a state transition from the lth bin to the mth one and $\Delta_m^{(\mathrm{h})}$ represents the set collecting the indices of the bins of the $(p-1)$th data block from which the mth bin can be reached in the pth data block. In our work, the following specific choices have been made:

a) The set

$$\Delta_m^{(\mathrm{h})} = \left\{\hat{n}_{\mathrm{min}}^{(\mathrm{h})}[m], \hat{n}_{\mathrm{min}}^{(\mathrm{h})}[m] + 1, \ldots, \hat{n}_{\mathrm{max}}^{(\mathrm{h})}[m]\right\} \tag{43}$$

has been chosen; here,

$$\hat{n}_{\mathrm{min}}^{(\mathrm{h})}[m] \triangleq \max\left\{n_{\mathrm{min}}^{(\mathrm{h})}, m - L_{\mathrm{h}}\right\} \tag{44}$$

and

$$\hat{n}_{\mathrm{max}}^{(\mathrm{h})}[m] \triangleq \min\left\{n_{\mathrm{min}}^{(\mathrm{h})} + N_{\mathrm{h}} - 1, m + L_{\mathrm{h}}\right\} \tag{45}$$

are the minimum and maximum bin indices, respectively, of the bins in the $(p-1)$th data block from which the mth bin in the pth data block can be reached, L_{h} is a positive integer defining the maximum size of the set $\Delta_m^{(\mathrm{h})}$ (which, at most, consists of $2L_h + 1$ consecutive integers).

b) The state transition probability $\beta_{m|l}^{(\mathrm{h})}$ has been evaluated as[10]

$$\beta_{m|l}^{(\mathrm{h})} = \mathcal{N}(m; l, \sigma_{\mathrm{h}}^2), \tag{46}$$

where $\mathcal{N}(x; \mu, \sigma^2)$ denotes the probability density function of a Gaussian random variable having mean and variance equal to μ and σ^2, respectively.

On the other hand, the *measurement update* of our filtering method is expressed by

$$\alpha_n^{(\mathrm{h})}[p] = \gamma_n^{(\mathrm{h})}[p] \frac{\hat{\alpha}_n^{(\mathrm{h})}[p]}{\sum_{l \in \mathcal{A}_{\mathrm{h}}} \hat{\alpha}_l^{(\mathrm{h})}[p]}, \tag{47}$$

with $n \in \mathcal{A}_{\mathrm{h}}$; here, $\gamma_n^{(\mathrm{h})}[p]$ denotes the probability that, based on the SFEC output available for the pth data block (i.e., on the measurements available for the considered update), the HR falls in the nth frequency bin. In practice, this probability is evaluated as

$$\gamma_n^{(\mathrm{h})}[p] = f_p^{(\mathrm{h})}(n), \tag{48}$$

with $n \in \mathcal{A}_{\mathrm{h}}$. Here,

$$f_p^{(\mathrm{h})}(x) \triangleq \sum_{i=1}^{\bar{M}_{\mathrm{h}}} \omega_i^{(\mathrm{h})} \cdot \mathcal{N}\left(x; \mu_i^{(\mathrm{h})}[p], (\sigma_i^{(\mathrm{h})}[p])^2\right) \tag{49}$$

[9] Note that, since the HR is discretised, the estimation accuracy for this parameter is limited by the selected discretisation step, i.e., in practice, by the adopted spectral resolution.

[10] This choice is motivated in Section V.

is the probability density function describing a *Gaussian mixture* (GM) with $\bar{M}_{\rm h} \triangleq 2M_{\rm h}\bar{N}_{\rm RX}$ components, and $\omega_i^{(\rm h)}$, $\mu_i^{(\rm h)}[p]$ and $\sigma_i^{(\rm h)}[p]$ denote the (positive) weight, the mean and the standard deviation, respectively, of its ith component (note that the GM weights must satisfy the normalization condition $\sum_{i=1}^{\bar{M}_{\rm h}} w_i^{(\rm h)} = 1$). In our algorithm, the parameters of the GM (49) are evaluated as follows. First of all, the $\bar{M}_{\rm h}$-dimensional vector of absolute amplitudes

$$\bar{\mathbf{a}}_{\rm h}[p] = \left[\mathbf{a}_{\rm h}^{(\nu_0)}[p], \mathbf{a}_{\rm h}^{(\nu_1)}[p], \ldots, \mathbf{a}_{\rm h}^{(\nu_{\bar{N}_{\rm RX}-1})}[p], \mathbf{a}_{\rm h}^{(\nu_0)}[p], \mathbf{a}_{\rm h}^{(\nu_1)}[p], \ldots, \mathbf{a}_{\rm h}^{(\nu_{\bar{N}_{\rm RX}-1})}[p]\right] \quad (50)$$

and the $\bar{M}_{\rm h}$-dimensional vector of normalised frequencies

$$\bar{\mathbf{F}}_{\rm h}[p] = \left[\mathbf{F}_{\rm h}^{(\nu_0)}[p], \mathbf{F}_{\rm h}^{(\nu_1)}[p], \ldots, \mathbf{F}_{\rm h}^{(\nu_{\bar{N}_{\rm RX}-1})}[p], 0.5\,\mathbf{F}_{\rm h}^{(\nu_0)}[p], 0.5\,\mathbf{F}_{\rm h}^{(\nu_1)}[p], \ldots, 0.5\,\mathbf{F}_{\rm h}^{(\nu_{\bar{N}_{\rm RX}-1})}[p]\right], \quad (51)$$

are generated. In particular, $\bar{\mathbf{a}}_{\rm h}[p]$ collects the absolute amplitudes estimated by the SFEC in the considered frequency range followed by a repetition of the same values, whereas $\bar{\mathbf{F}}_{\rm h}[p]$ collects the normalised frequencies estimated by the SFEC in the considered frequency range followed by a repetition of the same values divided by two. Then, the mean and the variance of the ith component of $f_p^{(\rm h)}(x)$ (49) are evaluated as

$$\mu_i^{(\rm h)}[p] = \bar{F}_i^{(\rm h)}[p]N_0' \quad (52)$$

and

$$(\sigma_i^{(\rm h)}[p])^2 = \alpha_{\rm h}\left[(1-\eta)\frac{\bar{a}_i^{(\rm h)}[p] - \bar{a}_{\rm min}^{(\rm h)}[p]}{\bar{a}_{\rm max}^{(\rm h)}[p] - \bar{a}_{\rm min}^{(\rm h)}[p]} + \eta\right]^{-1}, \quad (53)$$

respectively, with $i = 1, 2, \ldots, \bar{M}_{\rm h}$; here, $\bar{F}_i^{(\rm h)}[p]$ and $\bar{a}_i^{(\rm h)}[p]$ denote the ith element of $\bar{\mathbf{F}}_{\rm h}[p]$ (51) and $\bar{\mathbf{a}}_{\rm h}[p]$ (50), respectively, $\bar{a}_{\rm max}^{(\rm h)}[p] \triangleq \max \bar{\mathbf{a}}_{\rm h}[p]$, $\bar{a}_{\rm min}^{(\rm h)}[p] \triangleq \min \bar{\mathbf{a}}_{\rm h}[p]$, $\alpha_{\rm h}$ is a positive scale factor and η is a positive parameter (dubbed *range control parameter*) ensuring that the range of the denominator of the fraction appearing in the RHS of (53) is the interval $[\eta, 1]$ ($0 < \eta < 1$ is selected). Once the measurement update has been carried out, the index of the most likely state (i.e., frequency bin) is computed as

$$\hat{n}^{(\rm h)}[p] = \arg\max_{l \in \mathcal{A}_{\rm h}} \alpha_l^{(\rm h)}[p] \quad (54)$$

and the estimate

$$\hat{f}_{\rm h}[p] = \frac{\hat{n}^{(\rm h)}[p]}{T_{\rm SF}} \quad (55)$$

of the HR is evaluated on the basis of that index.

The filtering algorithm is initialised by setting

$$\alpha_n^{(\rm h)}[-1] = \frac{1}{N_{\rm h}} \quad (56)$$

for $n \in \mathcal{A}_{\rm h}$.

6) *Breath rate estimation* - The aim of the *sixth* block of Fig. 7 is BR estimation. The algorithm we developed for this task is fed by the set $\bar{\mathcal{S}}_{\rm b}[p]$ (39) and the apnea indicator $\xi[p]$ (40). Its structure is similar to that illustrated above for HR estimation; the main differences between it and the previous algorithm are summarised below.

a) The BR over each data block is represented as a *discrete state variable* that, however, can take on $N_{\rm b}$ distinct integer values and, in particular, any value of the set $\mathcal{A}_{\rm b} = \{n_{\rm min}^{(\rm b)}, n_{\rm min}^{(\rm b)} + 1, \ldots, n_{\rm min}^{(\rm b)} + N_{\rm b} - 1\}$; such values represent the indices of the $N_{\rm b}$ frequency bins falling in the frequency range $[f_{\rm b,min}, f_{\rm b,max}]$.

b) The amplitude vector $\bar{\mathbf{a}}_{\rm h}[p]$ (50) and the frequency vector $\bar{\mathbf{F}}_{\rm h}[p]$ (51) are replaced by the corresponding $M_{\rm b}\bar{N}_{\rm RX}$-dimensional vector of absolute amplitudes

$$\bar{\mathbf{a}}_{\rm b}[p] = \left[\mathbf{a}_{\rm b}^{(\nu_0)}[p], \mathbf{a}_{\rm b}^{(\nu_1)}[p], \ldots, \mathbf{a}_{\rm b}^{(\nu_{\bar{N}_{\rm RX}-1})}[p]\right] \quad (57)$$

and $M_{\rm b}\bar{N}_{\rm RX}$-dimensional vector of normalised frequencies

$$\bar{\mathbf{F}}_{\rm b}[p] = \left[\mathbf{F}_{\rm b}^{(\nu_0)}[p], \mathbf{F}_{\rm b}^{(\nu_1)}[p], \ldots, \mathbf{F}_{\rm b}^{(\nu_{\bar{N}_{\rm RX}-1})}[p]\right], \quad (58)$$

respectively. Note that the FH of the breath is always stronger than the associated SH; for this reason, there is no need to take into account the spectral contribution of the last harmonic.

c) The set $\Delta_m^{(\rm h)}$ (43) and the state transition probability $\beta_{m|l}^{(\rm h)}$ (46) are replaced by

$$\Delta_m^{(\rm b)} = \left\{\hat{n}_{\rm min}^{(\rm b)}[m], \hat{n}_{\rm min}^{(\rm b)}[m] + 1, \ldots, \hat{n}_{\rm max}^{(\rm b)}[m]\right\} \quad (59)$$

and

$$\beta_{m|l}^{(\rm b)} = \mathcal{N}(m; l, \sigma_{\rm b}^2), \quad (60)$$

respectively; here,

$$\hat{n}_{\rm min}^{(\rm b)}[m] \triangleq \max\left\{n_{\rm min}^{(\rm b)}, m - L_{\rm b}\right\}, \quad (61)$$

$$\hat{n}_{\rm max}^{(\rm b)}[m] \triangleq \min\left\{n_{\rm min}^{(\rm b)} + N_{\rm b} - 1, m + L_{\rm b}\right\} \quad (62)$$

and $L_{\rm b}$ is a positive integer defining the maximum size of the set $\Delta_m^{(\rm b)}$ (which, at most, consists of $2L_{\rm b} + 1$ consecutive integers). Note that, in general, the variance $\sigma_{\rm b}^2$ and the parameter $L_{\rm b}$ are different from their counterparts $\sigma_{\rm h}^2$ and $L_{\rm h}$ appearing in (44)-(45) and (46). This is due to the fact that, in general, the breath variability observed for a given subject always differs from his/her heart variability. Furthermore, HR is beyond the subject's control, while BR is not.

d) The probability $\gamma_n^{(\rm b)}[p]$ that BR belongs to the nth frequency bin is evaluated as

$$\gamma_n^{(\rm b)}[p] = f_p^{(\rm b)}(n), \quad (63)$$

where

$$f_p^{(\rm b)}(x) \triangleq \sum_{i=1}^{\bar{M}_{\rm b}} \omega_i^{(\rm b)} \cdot \mathcal{N}\left(x; \mu_i^{(\rm b)}[p], (\sigma_i^{(\rm b)}[p])^2\right) \quad (64)$$

is the probability density function describing a GM with $\bar{M}_{\rm b} \triangleq M_{\rm b}\bar{N}_{\rm RX}$ components, and $\omega_i^{(\rm b)}$, $\mu_i^{(\rm b)}[p]$ and $\sigma_i^{(\rm b)}[p]$ denote the (positive) weight, the mean and the standard deviation, respectively, of its ith component (note that the GM weights must satisfy the condition $\sum_{i=1}^{\bar{M}_{\rm b}} w_i^{(\rm b)} = 1$). The mean $\mu_i^{(\rm b)}[p]$ and the variance $(\sigma_i^{(\rm b)}[p])^2$ of the ith component of $f_p^{(\rm b)}(x)$ are evaluated on the basis of (52) and (53), respectively, where, however, h is replaced by b.

e) The algorithm is initialised by setting

$$\alpha_n^{(\rm b)}[-1] = \frac{1}{N_{\rm b}} \tag{65}$$

for $n \in \mathcal{A}_{\rm b}$.

f) The BR estimate is forced to 0 Hz for the duration of an apnea event. In this case, the variable $\xi[p]$ (40) is set to one and the BR estimation algorithm stops. When the end of the apnea event is detected (i.e., when $\xi[n]$ is zero again), the BR estimation algorithm is initialised again (see (65)).

This concludes our description of the VSEADA; its steps are summarised in Algorithm 1. This algorithm deserves various relevant comments, which are listed below.

1) *Computation of the phase gradient* - As already mentioned above, the sequence $\{g_{0,p}^{(v)}[n]\}$ (see (28)) conveys information about the PG characterizing the sequence $\mathbf{s}_p^{(v)}$ and referring to its elements spaced apart by Δn. Further details about the main properties of PG are provided in Appendix B, where it is shown that: a) the computation of the sequence $\{g_{0,p}^{(v)}[n]\}$ simplifies the detection of the FH of heart and respiration by enhancing their spectral contribution; b) the selection of the imaginary part of $\{f_{0,p}^{(v)}[n]\}$ (28) aims at suppressing both the (undesired) even-order harmonics (which appear in its real part) and the DC component (see also [18, Sec. III,eq. (12)]).

2) *Spectral analysis and sparsification* - In our work, the value selected for the parameter $M_{\rm h}$ has been always larger than that selected for $M_{\rm b}$; this is due to the fact that the FH of respiration activity is usually characterised by a high SNR.

3) *Antenna selection* - The antenna selection criterion we adopted (see (37)) is not influenced by the specific characteristics of the measurement scenario (e.g., by the propagation environment, the characteristics of the monitored patient, and the radar positioning). Note also that the sets $\bar{\mathcal{S}}_{\rm h}[p]$ (38) and $\bar{\mathcal{S}}_{\rm b}[p]$ (39) do not convey phase information. This is due to the fact that the processing accomplished by the devised HR and BR estimators does not require combining the contributions of different RX antennas in a coherent fashion.

4) *Apnea detection* - The criterion for apnea detection is very simple and exploits the information provided by the selected $\bar{N}_{RX}$ RX antennas in a non-coherent fashion.

5) *Estimation of heart and breath rates* - The development of algorithms for HR and BR estimation has required various assumptions. It is important to point out that:

a) The models $\beta_{m|l}^{(\rm h)}$ (46) and $\beta_{m|l}^{(\rm b)}$ (60) for state transition probabilities have been selected on the basis of our experimental results; further details about this issue are provided in Sec. V-B.

b) The sets $\Delta_m^{(\rm h)}$ (43) and $\Delta_m^{(\rm b)}$ (59), and the state transition probabilities $\beta_{m|l}^{(\rm h)}$ (46) and $\beta_{m|l}^{(\rm b)}$ (60) do not evolve over time. This assumption is reasonable when vital signs are estimated for a patient at rest.

c) The formula (53) adopted for the evaluation of the variance $(\sigma_i^{(\rm h)}[p])^2$ of the ith component of the GM (49) is motivated by the fact that a small spectral peak is associated with a low SNR and, consequently, with a large uncertainty; similar considerations holds for the evaluation of $(\sigma_i^{(\rm b)}[p])^2$. The implications of this choice are exemplified by Figs. 8a and 8b. More specifically, the first figure shows the amplitude spectrum of the PG for a specific RX antenna selected by the VSEADA and the $M_{\rm h} = 5$ peaks detected by the SFEC algorithm in the HR range. The second figure, instead, shows the GM generated on the basis of the output of the VSEADA and under the assumptions that its components have the same weight; note that weaker spectral peaks appearing in the first figure lead to wider Gaussian components. Further information about the considered example are provided in Table 2, in which the normalised frequency and amplitude of each spectral peak, and the mean and the variance of each of the $2M_{\rm h} = 10$ components of the associated GM are listed.

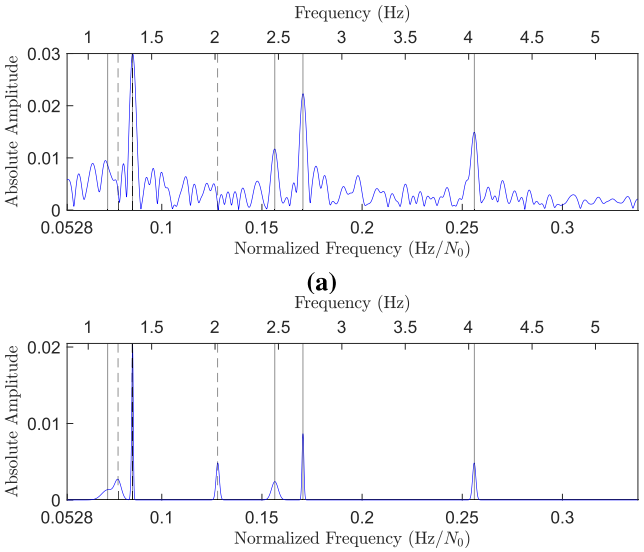

FIGURE 8. Representation of: (a) the amplitude spectrum of the PG computed over a data block on one of the RX antennas selected by the VSEADA (the vertical solid and dashed lines indicate the positions of the five dominant spectral components detected and estimated by the SFEC algorithm in the frequency range analysed for heart estimation and their positions divided by two, respectively); (b) the corresponding GM generated by the VSEADA (see (49)) under the assumption that $w_i^{(\rm h)} = 1/10$ for $i = 1, 2, \ldots, 10$, and on the basis of the means and variances listed in Table 2.

IV. COMPARISON WITH OTHER ESTIMATION METHODS

In this section, we first illustrate the architecture of two known methods for the estimation of vital signs, namely the AD and the CPG method. Then, we describe a new MCPG for the simultaneous estimation of BR and HR. Finally,

Algorithm 1 Vital Signs Estimation and Apnea Detection Algorithm (VSEADA)

Input: The integer parameters N_B, N_s, Δn, N_0', M_h and M_b, the real parameters α_h, α_b and η, and the sets $\{\mathbf{s}^{(v)}; v = 0, 1, \ldots, \tilde{N}_{RX} - 1\}$ (see (21)), $\mathcal{A}_h$ (see (41)), $\mathcal{A}_b$, $\{\omega_i^{(h)}\}$, $\{\omega_i^{(b)}\}$, $\{\beta_{m|l}^{(h)}\}$ and $\{\beta_{m|l}^{(b)}\}$ (see (46) and (60), respectively).

Initialization: Initialize $\{\alpha_n^{(h)}[-1]\}$ and $\{\alpha_n^{(b)}[-1]\}$ according to (56) and (65), respectively.

Main: for $p = 0$ *to* $(N_F - N_B)/N_s$ **do**

- **a-** Compute $\{\mathbf{g}_{0,p}^{(v)}\}$ (27) on the basis of (28)-(29).
- **b-** Evaluate $\{\mathbf{g}_{1,p}^{(v)}, \mathbf{g}_{2,p}^{(v)}\}$ (30) and $\{\mathbf{G}_q^{(v)}\}$ (32) according to (31) and (33), respectively. Then, generate $\{\mathbf{F}_x^{(v)}[p]\}$ (34) and $\{\mathbf{A}_x^{(v)}[p]\}$ (35), with x = b and h.
- **c-** Generate $\{Q^{(v)}[p]\}$ on the basis of (37).
- **d-** Compute $\xi[p]$ according to (40).
- **if** $\xi[p] == 1$ **then**
  - **e-** set $\hat{f}_b[p] = 0$ and evaluate $\{\alpha_n^{(b)}[p]\}$ on the basis of (65).
- **else**
  - **f-** Evaluate $\{\hat{\alpha}_m^{(b)}[p]\}$ (see (42)).
  - **g-** Compute $\{\mu_i^{(b)}[p]\}$ and $\{(\sigma_i^{(b)})^2\}$ (see (52) and (53), respectively). Then, evaluate $\{\gamma_n^{(b)}[p]\}$ and $\{\alpha_n^{(b)}[p]\}$ according to (63)-(64) and (47), respectively.
  - **h-** Evaluate $\hat{f}_b[p]$ according to (54)-(55).
- **end**
- **i-** Evaluate $\{\hat{\alpha}_m^{(h)}[p]\}$ on the basis of (42).
- **j-** Compute $\{\mu_i^{(h)}[p]\}$ and $\{(\sigma_i^{(h)})^2\}$ on the basis of (52) and (53), respectively. Then, evaluate $\{\gamma_n^{(h)}[p]\}$ and $\{\alpha_n^{(h)}[p]\}$ according to (48)-(49) and (47), respectively.
- **k-** Evaluate $\hat{f}_h[p]$ according to (54)-(55).

end

Output: $\{\hat{f}_h[p]; p = 0, 1, \ldots, (N_F - N_B)/N_s\}$ and $\{\hat{f}_b[p]; p = 0, 1, \ldots, (N_F - N_B)/N_s\}$.

we discuss the pros and cons of both methods and compare them with the VSEADA.

In our description of the AD and the MCPG methods, we assume that the measurements for VSM originate from a *single* SIMO radar device, equipped with N_{RX} RX antennas. In this case, one of the following two options, both widely employed in the technical literature, can be adopted to benefit from the availability of multiple RX antennas:

a) *Beamforming* - This strategy allows enhancing the overall SNR by constructively combining the echoes impinging on the RX array along a specific direction (e.g., see [15], [32], [33]).

b) *Random antenna selection* - In this case, a MIMO radar is used as a SISO one, since all the measurements are acquired from a single virtual antenna, that is randomly

TABLE 2. Values of the normalised frequency and amplitude characterizing the five spectral peaks highlighted in Fig. 8a. The means $\{\mu_i^{(h)}\}$ and variances $\{(\sigma_i^{(h)})^2\}$ of the ten components of the GM generated on the basis of these results and (52)-(53) are also listed.

Norm. frequency		Amplitude			
Symbol	Value	Symbol	Value	$\mu_i^{(h)}$	$(\sigma_i^{(h)})^2$
$\mathbf{F}_h$	0.085	$\mathbf{A}_h$	$0.029 - j0.007$	860	3.000
	0.17		$0.014 + j0.017$	1714	4.602
	0.256		$-0.007 + j0.014$	2573	8.229
	0.156		$0.001 + j0.011$	1573	16.650
	0.073		$-j0.009$	735	30.000
$\mathbf{F}_h/2$	0.043	$\mathbf{A}_h$	$0.029 - j0.007$	430	3.000
	0.085		$0.014 + j0.017$	857	4.602
	0.128		$-0.007 + j0.014$	1286.5	8.229
	0.078		$0.001 + j0.011$	786.5	16.650
	0.037		$-j0.009$	367.5	30.000

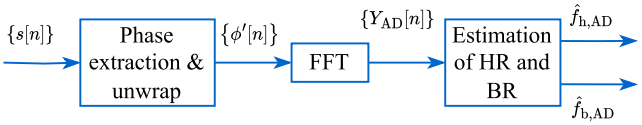

FIGURE 9. Architecture of the *arctangent demodulator*.

selected and maintained for the whole acquisition [14], [18]. This simplifies processing, at the expense of worse performance, since the system does not benefit from the potentially available spatial diversity.

In both cases, the set $\{x^{(v)}[k, s, n]\}$ (see (6)) is replaced by the set $\{x[k, s, n]\}$, with

$$x[k, s, n] \simeq a[s] \exp(j(2\pi k f_n T_s + \psi[s, n])) + w[k, s, n] \tag{66}$$

for any s, k and n. Moreover, the first three steps described for the VSEADA (see Sec. III), namely coherent combining, target detection, and extraction of relevant spectral information, are also executed by the AD and the CPG (MCPG) method. Their input is represented by the set $\{x[k, s, n]\}$, whereas their output is the sequence $\{s[n]\}$, with (see (21))

$$s[n] = b \exp(j\phi[n]) + w_R[n]. \tag{67}$$

with $n = 0, 1, \ldots, N_F - 1$. The remaining steps are illustrated in the following two subsections for each of the considered methods. In our description, we focus on the processing accomplished on a single data block collecting the measurements $\{s[n]; n = 0, 1, \ldots, N_B - 1\}$.

A. ARCTANGENT DEMODULATION

The AD has been originally proposed by Park et al. in 2007 [7] to circumvent the problem of the null detection point in VSM through microwave Doppler radars. Because of its technical relevance, its accuracy has been widely assessed in the technical literature (e.g., see [9], [16], [18], [28], [42], [43]). Luckily, modern mm-wave radars employed in the recent literature on VSM do not suffer from the above-mentioned problem since they are equipped with balanced quadrature receivers. Despite this, the use of the

AD method is still justified, since vital signs information is embedded in the phase of the received signal (see (67)) and the AD acquires that information from the unwrapped phase which is extracted from the range bin of the detected target (this bin is selected according to (19)-(20); see Sec. II). The processing accomplished by the AD is described by the block diagram shown in Fig. 9 and can be summarised as follows.

1) *Phase extraction & unwrapping* - The sequence $\{s[n]; n = 0, 1, \ldots, N_B - 1\}$ undergoes phase extraction followed by unwrapping. Phase extraction produces the sequence $\{\phi[n]; n = 0, 1, \ldots, N_B - 1\}$, consisting of N_B phases; here, for any n,

$$\phi[n] \triangleq \arctan\left(\frac{s^{(Q)}[n]}{s^{(I)}[n]}\right), \tag{68}$$

$s^{(Q)}[n] \triangleq \Im\{s[n]\}$ and $s^{(I)}[n] \triangleq \Re\{s[n]\}$. Then, the unwrapping of $\phi[n]$ gives

$$\phi'[n] = \begin{cases} \phi[n], & \text{if } |\phi[n] - \phi[n-1]| \leq \pi \\ \phi[n] - 2\pi, & \text{if } \phi[n] - \phi[n-1] > \pi \\ \phi[n] + 2\pi, & \text{if } \phi[n] - \phi[n-1] < -\pi. \end{cases} \tag{69}$$

for $n = 0, 1, \ldots, N_B - 1$.

2) *Spectral analysis* - The sequence $\{\phi'[n]; n = 0, 1, \ldots, N_B - 1\}$ undergoes zero padding followed by order N_0' FFT processing; here, $N_0' \triangleq N_B \cdot M'$, where M' is the adopted oversampling factor. This generates the sequence $\{Y_{AD}[n]; n = 0, 1, .., N_0' - 1\}$, collecting N_0' spectral samples.

3) *Estimation of heart and breath rates* - The indices

$$\hat{h}_{b,AD} = \arg \max_{\tilde{h}_b \in \left\{h_{min}^{(b)}, \ldots, h_{max}^{(b)}\right\}} |Y_{AD}[\tilde{h}_b]| \tag{70}$$

and

$$\hat{h}_{h,AD} = \arg \max_{\tilde{h}_h \in \left\{h_{min}^{(h)}, \ldots, h_{max}^{(h)}\right\}} |Y_{AD}[\tilde{h}_h]| \tag{71}$$

of the two highest peaks, one in the BR region, the other one in the HR region, respectively, are searched for; here, $h_{min}^{(b)}$ ($h_{min}^{(h)}$) and $h_{max}^{(b)}$ ($h_{max}^{(h)}$) are the minimum and maximum bin indices for BR (HR) estimation. Based on the index of these peaks, the BR estimate and the HR estimate are evaluated as

$$\hat{f}_{b,AD} = \frac{\hat{h}_{b,AD}}{N_0' T_F} \tag{72}$$

and

$$\hat{f}_{h,AD} = \frac{\hat{h}_{h,AD}}{N_0' T_F}, \tag{73}$$

respectively.

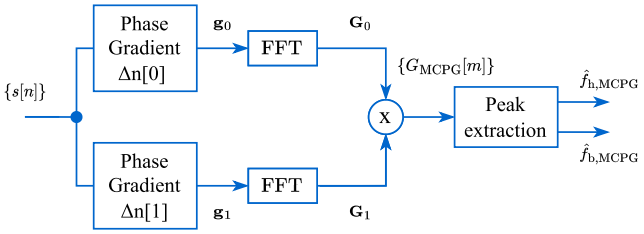

FIGURE 10. Architecture of the *cumulative phase gradient* method for $L = 2$.

B. CUMULATIVE PHASE GRADIENT METHOD

The CPG method, employing the PG operation, has been recently developed by Wu et al. [18] for estimating the BR of *multiple* closely spaced subjects. In our work, we have investigated the possibility of modifying this method [18] for the estimation of both the HR and BR of a *single* subject. Our attempt has been motivated by the fact that the PG spectrum contains multiple harmonics originating from both heart and respiration displacements, and has led to the development of the MCPG technique. The architecture of our MCPG method is described by the block diagram shown in Fig. 10. The processing accomplished by this method can be summarised as follows.

1) *Computation of phase gradient information* - PG information is extracted from the sequence $\{s[n]\}$ for L distinct time lags, denoted $\{\Delta n[l]; l = 0, 1, \ldots, L - 1\}$. For any l, the N_B-dimensional vector

$$\mathbf{g}_l \triangleq [g_l[0], g_l[1], \ldots, g_l[N_B - 1]]^T, \tag{74}$$

associated with the time lag $\Delta n[l]$ (additional details about the PG operation are provided in Appendix B), is evaluated. The nth element of the vector $\mathbf{g}_l$ (74) is evaluated as

$$g_l[n] \triangleq \Im\{f_l[n]\}, \tag{75}$$

where

$$f_l[n] \triangleq s[n] \cdot (s[n + \Delta n[l]])^*. \tag{76}$$

2) *Spectral analysis* - Each sequence of the set $\{\mathbf{g}_l; l = 0, 1, .., L - 1\}$ undergoes zero padding followed by order N_0' FFT processing; here, $N_0' \triangleq (N_B - \Delta n[l]) \cdot M'$, where M' is the adopted oversampling factor. This generates the sequences

$$\mathbf{G}_l \triangleq [G_l[0], G_l[1], \ldots, G_l[N_0' - 1]]^T, \tag{77}$$

for $l = 0, 1, .., L - 1$, each collecting N_0' spectral coefficients ($\mathbf{G}_l$ denotes the output of the FFT fed by the zero-padded version of $\mathbf{g}_l$).

3) *Fusion of spectral information* - The new sequence $\{G_{MCPG}[m]; m = 0, 1, \ldots, N_0' - 1\}$ is generated by merging the L sequences $\{\mathbf{G}_l; l = 0, 1, .., L - 1\}$; here,

$$G_{MCPG}[m] \triangleq \prod_{l=0}^{L-1} G_l[m] \tag{78}$$

for any m.

4) *Estimation of heart and breath rates* - The two highest peaks, one in the HR region and the other one in the BR

region, are searched for in the sequence $\{|G_{\mathrm{MCPG}}[m]|;\, m = 0, 1, .., N_0' - 1\}$ (see (70)-(71)). Based on the index of these peaks, the HR estimate $\hat{f}_{\mathrm{h,MCPG}}$ and the BR estimate $\hat{f}_{\mathrm{b,MCPG}}$ are evaluated according to (72) and (73), respectively.

Finally, it is important to point out that, in our work, we have also taken into consideration the possibility of using the HSPG method described in [20]. However, the HR estimation algorithm exploited by that method requires a frame rate substantially higher than that available in the radar systems employed in our experiments.[11] For this reason, the HSPG method is not considered again in the remaining part of this manuscript.

C. COMPARISON

All the estimation methods described in the previous two subsections consist of a pre-processing part followed by spectral analysis. Despite their similarities, they have various limitations, as illustrated below.

First of all, the AD suffers from the following problems:

Estimation errors due to phase unwrapping - The phase unwrapping operation, expressed by (69), is a non-linear operation introducing errors whenever the absolute value of the difference between the phases of two consecutive elements of the sequence $\{s[n]\}$ is larger than 2π [44]. Unwrapping errors are likely to happen in the presence of noise, multipath, and RBMs [9], [45].

Presence of a direct current component - A strong DC is typically present in the unwrapped sequence $\{\phi'[n]\}$ (69). This term originates not only from electronic components, but also from the signal reflected by stationary objects and other parts of the human body different from the chest wall. Note that the sequence $\{\phi'[n]\}$ undergoes band-pass filtering to cancel all the spectral components whose frequency falls outside the interval in which the heart frequency and breath frequency are expected [4, Sec. VA].

Estimation errors due to the harmonics of respiration activity - The spectral peaks associated with the harmonics of breath and lying in the frequency range $[f_{\mathrm{h,min}}, f_{\mathrm{h,max}}]$ are usually higher than the peak characterizing the FH of heart.[12] When this occurs, an erroneous estimate of HR is generated (see (71)). In principle, this problem could be solved by first estimating the FH of respiration activity, and then detecting, estimating and cancelling all the relevant harmonics[13] falling in the frequency range $[f_{\mathrm{h,min}}, f_{\mathrm{h,max}}]$. However, our experimental results have evidenced that, in some cases, the HR coincides with (or is extremely close to) a multiple of BR; therefore, the cancellation of breath harmonics may lead to the total or partial cancellation of the (small) spectral peak appearing at HR.

The MCPG method offers various advantages with respect to the AD, since: a) in principle, the PG evaluated according to (28) does not contain breath and heart even harmonics and a DC component (see Appendix B); b) it mitigates the impact of measurement noise, thanks to its fusion of spectral information (see (78)), that enhances the spectral peaks appearing in all the spectra while attenuating those not having this property [18].

The VSEADA, being based on the PG, benefits from all the advantages offered by the MCPG method. However, unlike the MCPG method, it is able to: a) mitigate the impact of multipath through a simple selection combining strategy; b) reduce the impact of RBM through the use of a novel filtering method; c) detect apnea events. Moreover, the VSEADA, unlike the two methods described above, is able to exploit the heart SH in the estimation of HR; this significantly improves the reliability and accuracy of its HR estimates.

The considered estimation methods are listed in Table 3, where the following specific features are specified for each of them: a) the absence of HOH and intermodulation products in the spectral information exploited for the estimation of BR and HR; b) the ability to mitigate the impact of measurement noise; c) the ability to mitigate RBM; d) the apnea detection capability; e) the exploitation of heart SH in HR estimation.

The last issue considered in this subsection concerns the computational effort required by all the above mentioned estimation methods. A detailed derivation of their computational complexities is illustrated in Appendix C. The order of the computational complexity for each method is summarised in Table 4, where the number of flops executed in processing a single data block is specified. These results are easily obtained from the expressions we derived for the computational complexity of the VSEADA, the AD and the MCPG method (see (104), (107) and (110), respectively). In doing so, the following considerations have been made: a) the difference $(l_{\max} - l_{\min})$ is in the order of a few tens; b) the value of N_{C} is smaller than 10; c) N_{RX} is equal to 2 in our experimental setup (see Sec. V); d) the SFEC computational complexity is on the order of that of a single FFT only [21] (in other words, $\mathcal{C}_{\mathrm{SFEC}} \approx (N_0' \log_2 N_0')N_{\mathrm{RX}}$); e) the values of M_{h} and M_{b} are in the order of a few units. From Table 4, it can be inferred that: a) the complexity of the AD is similar and significantly lower than those of the MCPG method and the VSEADA, respectively; b) the VSEADA is the method having the highest complexity.

V. NUMERICAL RESULTS

The aim of this section is threefold. First, we describe the experimental setup developed for acquiring vital sign information through SIMO radars and reference sensors. Next, we highlight some key insights we gained from analyzing our experimental results. Finally, we compare the

[11] Heart rate estimation is based on eq. (13) appearing in Subsec. II-C of [20]. The time delay $\Delta\tau$ must be carefully selected for cancelling the contributions due to respiration in the function to be maximized for HR estimation. Unluckily, in practice, the value of $\Delta\tau$ cannot be arbitrarily selected, since it is constrained to be a multiple of the sampling period.

[12] In principle, multiple breath harmonics may fall in the frequency range of heart. For example, in the worst case scenario, i.e. if $f_{\mathrm{b}} = f_{\mathrm{b,max}} = 0.5$, the second, third, fourth, and fifth harmonics of respiration fall in the HR region. However, only the harmonics up to the fourth one are usually stronger than the heart FH.

[13] This task can be accomplished through various frequency estimators based on a sequential cancellation approach (e.g., see [37] and references therein).

TABLE 3. Main features of the considered radar-based methods for VSM.

Feature	AD	MCPG	VSEADA
Absence of HOH and intermodulation		✓	✓
Noise mitigation		✓	✓
RBM mitigation			✓
Apnea detection			✓
Exploitation of heart SH			✓

TABLE 4. Computational complexity order of the considered estimation algorithms.

Algorithm	$\mathcal{O}(\cdot)$
AD	$\mathcal{O}((2NN_{\mathrm{C}}N_{\mathrm{RX}} + N_0 \log_2 N_0)N_{\mathrm{F}} + N'_0 \log_2 N'_0)$
MCPG	$\mathcal{O}((2NN_{\mathrm{C}}N_{\mathrm{RX}} + N_0 \log_2 N_0)N_{\mathrm{F}} + LN'_0 \log_2 N'_0)$
VSEADA	$\mathcal{O}(\left[(2NN_{\mathrm{C}} + N_0 \log_2 N_0)\, N_{\mathrm{F}} + N'_0 \log_2 N'_0\right] \tilde{N}_{\mathrm{RX}})$

VSEADA with the AD and MCPG methods in terms of estimation accuracy and computational efficiency.

A. EXPERIMENTAL SETUP

The performance of the considered VSM algorithms has been assessed on the basis of the measurements acquired through a couple of *Position2Go* radars [46]. These devices, manufactured by Infineon, operate at the frequency $f_0 = 24$ GHz, and are equipped with a single TX antenna and a couple of RX antennas ($N_{\mathrm{RX}} = 2$). In our work, the following values have been selected for the parameters of each radar device: 1) chirp slope $\mu = 0.78$ MHz/μ s; 2) overall number of samples per chirp $N = 256$; 3) ADC sampling rate $f_{\mathrm{s}} = 1$ MHz; 4) chirp duration interval $T_0 = 456$ μ s; 5) frame duration $T_{\mathrm{F}} = 0.063$ s; 6) number of Doppler chirps per frame $N_{\mathrm{C}} = 3$. Note that, in this case, the ramp-up time is $T = N/f_{\mathrm{s}} = 256$ μ s and the bandwidth of the radiated signal is $B = 200$ MHz.

The two radar devices have been mounted on a stand, in a non-planar[14] configuration and spaced 0.2 m apart, approximately at 1 m distance in front of the subject to be monitored, as shown in Fig. 11. In the case of the VSEADA, these devices operate in round robin fashion. In fact, the first chirp of each frame radiated by the second radar is triggered after the end of the transmission of the last chirp of the frame sent by the first radar. This ensures that the chirps of each radar are sent and received during the idle time interval (lasting T_{I}) of the other one; this is exemplified in Fig. 4. The VSEADA selects two of the four signals provided by all the RX antennas (i.e., $\bar{N}_{\mathrm{RX}} = 2$). In the case of the AD and CPG, instead, the measurements to be processed originate from a single radar device,[15] which is selected at the beginning of data acquisition and is never changed; here, beamforming (see Sect. IV) is employed to combine the signal from the two RX antennas.

[14]The non-planarity of the employed radar boards allows to better exploit spatial diversity, so mitigating the impact of the multipath phenomenon.

[15]Note that each of the considered algorithms process the measurements provided by two RX antennas.

A reference sensor, namely the *Shimmer3 ECG Unit* device [47], has also been used to acquire an accurate estimate of vital signs. This FDA-approved device, manufactured by Shimmer Research Ltd, makes use of a Bluetooth radio interface to transmit the acquired measurements and is equipped with five electrodes, which need to be placed in specific positions on the chest of the subject under test. In our acquisitions, the reference ECG signal has been read from the voltage difference between the left leg and RHS midaxillary (LL-RA) electrodes. The breathing signal, instead, has been generated by measuring the impedance between these two electrodes. The time-domain signals sent through the Bluetooth interface have undergone the standard *Pan–Tompkins algorithm* [48] (unluckily, apnea events cannot be detected). Due to the availability of a proper *application programming interface* (API), Shimmer3 measurements can be easily synchronised in time with those acquired through the radar devices, so that data acquisition can be accomplished in real time. In fact, the Shimmer3 device can share its time reference (namely, the *central processing unit* (CPU) timestamp) with the radar devices; this has allowed us to synchronize the reference sensor and the radars with high accuracy.

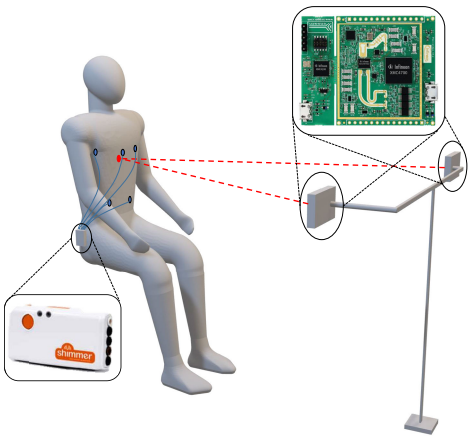

FIGURE 11. Representation of the adopted measurement setup: two Position2Go radars, installed on a stand, are put in front of the subject to be monitored. The Shimmer3 ECG Unitis used as reference sensor.

Our experimental campaign, conducted on 8 volunteers, enabled us to acquire a set of radar measurements and of the corresponding reference signals in the following two scenarios: a) Under *non-apneic conditions* (NAC): For each subject, measurements lasting approximately 60 seconds each were acquired at three different positions using our radar-based VSM system. In particular, the positions shown in Fig. 12 and denoted P1, P2 and P3, have been considered. In the case of P1 and P3, the system was aligned with the chest of the monitored subject and its stand centre was at a distance of 1 m and 2 m, respectively. In the case of P2, instead, the system was at the same distance as P1, but had undergone a 30° clockwise rotation. b) Under *apneic conditions* (AC),

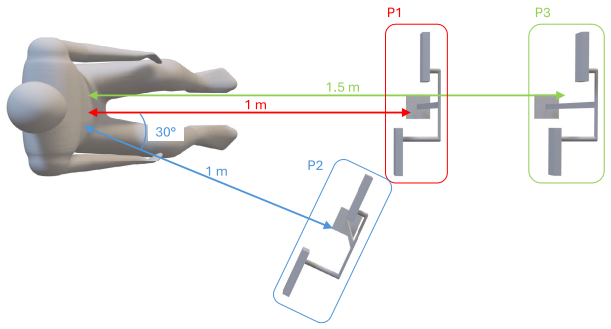

FIGURE 12. Representation of the three positions selected for the radar-based VSM system in the generation of our dataset: P1) the system is 1 m far from the chest of the monitored subject and aligned with his/her front; P2) the system is one meter far from his/her chest, but has undergone a 30° clockwise rotation with respect to the previous case; P3) the system is 1.5 m far from his/her chest and aligned with his/her front.

i.e., while experiencing apnea events of arbitrary duration[16] - For each subject, a single acquisition lasting approximately 180 s, was performed at position P1; moreover, multiple apnea events occurred during each measurement interval. Note that, in both scenarios, the overall duration of the available measurements was 1440 s. The values selected for the parameters of the considered estimation algorithms are listed in Table 5. Based on these values and the formulas given in Table 4, it can be shown that the computational complexity of the AD and the MCPG method is in the order of 0.107 Gflops, whereas that of the VSEADA is in the order of 0.422 Gflops (i.e., is about four times larger). This computational gap has been confirmed by the duration of the time interval required for estimating HR and BR over a single data block through the MATLAB implementation of these algorithms, that have been executed on a PC equipped with an Intel Core I7-1165G7 CPU. In fact, the VSEADA has required approximately 0.17 s, whereas the AD and the MCPG method 0.04 s and 0.05 s, respectively.

B. KEY INSIGHTS DERIVED FROM OUR EXPERIMENTAL RESULTS

An in-depth analysis of our experimental results has evidenced the importance of various issues to be kept carefully in mind in radar-based estimation of vital signs. In this subsection we focus on four specific issues that we deem to be really significant in VSM.

a) *On the importance of the second harmonic in heart rate estimation*

As already mentioned in Sec. III, the spectral analysis of our acquisitions has evidenced that heart SH is sometimes stronger than the associated FH. This HR doubling effect [7] is clearly visible in Fig. 13, where the amplitude spectrum observed from a single RX antenna of each radar device is shown for a given acquisition from the dataset acquired under AC. In this case, any strategy based on the detection of spectral peaks (like the AD and MCPG methods) unavoidably

[16]In these acquisitions, the apnea events started at random instants.

TABLE 5. Values of the parameters selected for the HR and BR estimation algorithms considered in this manuscript.

Method	Parameter	Symbol	Value
All	Range oversampling factor	M	8
	Minimum range distance	$R_{\min}$	0.5
	Maximum range distance	$R_{\max}$	1.5
	Acquisition duration (no. of frames)	N_{F}	1000
	Data block size	N_{B}	317
	Data block shift	N_{s}	4
	Doppler oversampling factor	M'	32
VSEADA	Time lag	Δn	1
	Number of selected RX antennas	$\bar{N}_{RX}$	2
	Number of heart peaks	M_{h}	5
	Number of breath peaks	M_{b}	3
	Heart GM weights	$\omega_i^{(\mathrm{h})}$	0.05
	Breath GM weights	$\omega_i^{(\mathrm{b})}$	0.167
	Maximum heart deviation	L_{h}	12
	Maximum breath deviation	L_{b}	18
	Heart state transition variance	σ_{h}^2	0.00175
	Breath state transition variance	σ_{b}^2	0.00260
	Scale factor	α_{h}	3
	Scale factor	α_{b}	2
	Range control parameter	η	0.1
MCPG	Number of distinct time lags	L	2
	Time lags	$\Delta n[0]; \Delta n[1]$	1; 2

leads to an erroneous HR estimate. The VSEADA, instead, exploits the presence of the second harmonic to improve the reliability of HR estimates.

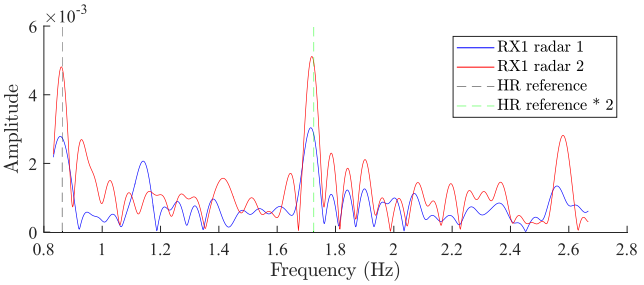

FIGURE 13. Representation of the amplitude spectrum observed on a single RX antenna of each radar device employed by the VSEADA. The SH of heart displacement is identified by the vertical green line (corresponding to a frequency equal to 1.72 Hz); its strength is significantly higher than that of the associated FH, which is identified by the black vertical line (corresponding to a frequency equal to 0.86 Hz.

b) *Impact of multipath on radar measurements*

Because of the multipath phenomenon and the small wavelength characterizing the employed radar devices, significant changes are observed in the quality of the signals received by different antennas [31]. This is exemplified by Fig. 14, where the amplitude spectra observed over the two RX antennas of the same radar device are shown. In fact, in this case, the amplitude spectrum referring to the RX antenna of the first radar is characterized by well-visible peaks in correspondence with the breath and heart FHs, whereas that referring to the RX antenna of the second radar is useless, since it does not exhibit significant peaks in the frequency range of interest. The same concept has also been exploited in [39] to select the range bins containing relevant vital signs information; in that work, the ratio between the in-band

energy (i.e., the energy obtained accumulating frequency responses within the respiration and heartbeat ranges) and the out-band energy was employed as an indicator. Note also that the quality metric (37) $Q^{(1)} = 5.06 \cdot 10^{-4}$ obtained for the first radar is significantly greater than its counterpart $Q^{(2)} = 6.56 \cdot 10^{-6}$ evaluated for the other radar.

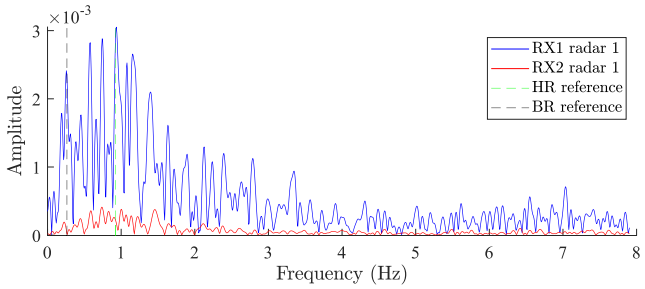

FIGURE 14. Representation of the amplitude spectra observed on the two RX antennas of a single radar. The black and green vertical lines identify the BR and HR, respectively, provided by the Shimmer3 device. The amplitude spectrum evaluated for the first RX antenna (blue line) exhibits well defined peaks centred in correspondence of the heart and respiration frequencies; the other amplitude spectrum (red line), instead, does not have this property and is deeply attenuated in the frequency range of interest.

c) *Apnea detection performance*

As illustrated in Sec. III, the VSEADA detects an apnea event when the most significant peak observed in the heart region is higher than its counterpart in the breath region. This is exemplified by Fig. 15, where the spectrum observed before an apnea event and that obtained during it on the same RX antenna are represented in blue and red, respectively. Note that the position of the peak corresponding to HR changes during this event (in particular, a physiological increase in HR is observed). Our experimental results over the AC dataset have also evidenced that: a) the *missed detection*[17] probability for apnea events during less than 15 seconds is approximately 0.15; otherwise, it is equal to zero; b) *false alarm* events are very unlikely (actually, no event of this type has been observed in our experiments); c) a time lag, spanning between 3 s and 15 s (with a mean equal to 10 s), is observed in apnea detection.

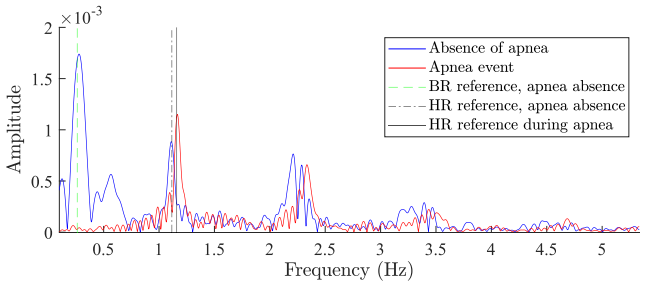

FIGURE 15. Representation of the apnea effects on the amplitude spectrum observed on a given RX antenna. The spectrum observed during apnea (red curve), contrarily to that referring to its absence (blue curve), is characterized by no BR peak (whose position is identified by the green vertical line).

[17]Missed detection corresponds to the case in which apnea is not detected over the entire event, nor immediately after that apnea has concluded.

d) *Variability of heart and breath rates under rest conditions*

The HR and BR signals acquired from the reference sensor (Shimmer3, see Subsec. V-A) over the entire NAC dataset have been employed to estimate the values of the following parameters: 1) heart state transition variance σ_{h}^2, employed in the evaluation of the heart state transition probability $\beta_{m|l}^{(\mathrm{h})}$ (46); 2) breath state transition variance σ_{b}^2, employed in the evaluation of the breath state transition probability $\beta_{m|l}^{(\mathrm{b})}$ (60); 3) the maximum heart deviation L_{h}, i.e. the maximum size of the set $\Delta_m^{(\mathrm{h})}$ (43); 4) the maximum breath deviation L_{b}, i.e. the maximum size of the set $\Delta_m^{(\mathrm{b})}$ (59).

The Matlab "Distribution Fitter" tool from the Statistics and Machine Learning Toolbox 12.4 has been employed to estimate the state transition variances; it has provided $\sigma_{\mathrm{h}}^2 = 1.75 \cdot 10^{-3}$ and $\sigma_{\mathrm{b}}^2 = 2.60 \cdot 10^{-3}$. Furthermore, our results have evidenced that, for $T_{\mathrm{SF}} = 0.063$ s, $L_{\mathrm{h}} = 12$ and $L_{\mathrm{b}} = 18$ should be selected for the maximum size of the sets $\Delta_m^{(\mathrm{h})}$ and $\Delta_m^{(\mathrm{b})}$, respectively.

e) *Impact of the position of the monitored subject and the environment*

The accuracy of vital sign estimation depends on the range and orientation of the monitored subject with respect to the employed radar device. It is important to keep in mind that the radar-target distance should not exceed the maximum range[18] of the employed device and, at the same time, should be large enough to guarantee that the measurements are not acquired in near-field conditions. To assess the impact of the radar-target distance on the performance of our VSM system, various measurements have been acquired at both the positions P1 and P3 shown in Fig. 12; in the next subsection we comment on what has emerged from them. Here, we just mention that the most important lessons that we learned from our measurement campaigns concern the impact of the position of the monitored subject in HR estimation. It is important to keep in mind that heartbeat vibrations propagate through the blood and vessels, so reaching the extremities of the human body [49]; for this reason, they can be detected at different points of the body. However, measurements of heart vibrations acquired from arms and legs may lead to poorer accuracy because of the increased susceptibility of these parts to RBMs. According to the scientific literature, the optimal detection of cardiac motion can be obtained by measuring the displacement at the sternum [39]. Nevertheless, as evidenced in [6], heart vibrations can be consistently captured as long as there is an unobstructed view between the radar front end and the patient's ribcage (i.e., arms or objects do not block the direct propagation path). Since our VSM system has no angle discrimination capability (beamforming is not employed), it captures any movement falling within the FOV of the employed radars. Consequently, moving or vibrating objects located within the FOV and at a comparable distance

[18]The maximum range, also called *maximum unambiguos range distance* [4], is about 96 m for the Position2Go if the values provided in Sec. V-A are selected for its parameters.

from the body may affect the quality of measurements. The FOV of the employed radars is 19° and 76° in elevation and azimuth, respectively, if the 3 dB *Half Power Beamwidth* is adopted to quantify it [46]. In our acquisitions, the radars have been positioned in front of the monitored subject in a way that their wider aperture illuminates the full height of his/her body; this choice ensures that the interference from objects at the comparable distance from the subject is minimized. The VSM system sensitivity to radar-chest alignment has been assessed through the acquisition of measurements at both the positions P1 and P2 (see Fig.12).

C. COMPARISON OF DIFFERENT ALGORITHMS

The estimation accuracy of the VSEADA has been compared with that achieved by the AD and the MCPG method. To this aim, the following three performance indices have been evaluated over the whole NAC dataset (see [4, eqs. (88)-(90)]) for the obtained HR and BR estimates: a) *root mean square error* (RMSE); b) *mean absolute error* (MAE), and; c) *peak absolute error* (PAE). Our numerical results referring to BR are listed in Table 6, whereas those referring to HR are listed in Table 7.

TABLE 6. Root mean square error, peak absolute error and mean absolute error evaluated for the BR estimates on the basis of the dataset acquired under NAC.

			Method		
Position	**FOM**	**m.u.**	AD	MCPG	**VSEADA**
P1	RMSE	acts/min	7.213	8.476	**4.822**
	MAE	acts/min	5.381	5.397	**1.529**
	PAE	acts/min	**16.572**	19.879	20.891
P2	RMSE	acts/min	8.069	5.649	**3.093**
	MAE	acts/min	7.098	2.600	**0.826**
	PAE	acts/min	**12.619**	19.387	16.820
P3	RMSE	acts/min	8.976	7.452	**3.336**
	MAE	acts/min	8.222	4.314	**0.951**
	PAE	acts/min	**15.725**	18.077	17.408

TABLE 7. Root mean square error, mean absolute error and peak absolute error evaluated for the HR estimates on the basis of the dataset acquired under NAC.

			Method		
Position	**FOM**	**m.u.**	AD	MCPG	**VSEADA**
P1	RMSE	bpm	17.9138	16.809	**7.649**
	MAE	bpm	12.960	10.786	**2.779**
	PAE	bpm	37.659	58.152	**27.938**
P2	RMSE	bpm	9.386	24.758	**1.762**
	MAE	bpm	6.643	15.850	**0.751**
	PAE	bpm	29.358	76.682	**26.148**
P3	RMSE	bpm	11.181	12.487	**3.394**
	MAE	bpm	8.019	7.471	**1.269**
	PAE	bpm	29.637	58.235	**23.420**

From these results it can be easily inferred that: a) the VSEADA outperforms the other two methods in BR estimation; b) a significant gap between the VSEADA and the other two methods is also observed in HR estimation, if RMSE and MAE are taken into consideration in this comparison; c) the VSEADA is outperformed by the AD in terms of PAE and for BR only; this is due to the occurrence of a small number of events in which the VSEADA exhibits a higher HR estimation error than that of the AD; d) vital signs can be estimated at all the considered positions, but the best accuracy it obtained at P2. The meaning of these results can be grasped by comparing the spectrograms exploited by the AD and MCPG methods for vital signs estimation with the time evolution of the probabilities $\{\alpha_n^{(\mathrm{x})}[p]; n = n_{\min}^{(\mathrm{b})}, \ldots, n_{\min}^{(\mathrm{b})} + N_{\mathrm{b}} - 1\}$ (with x = b and h for BR and HR estimation, respectively), i.e., briefly, with the *probability map* generated by the VSEADA. Some results referring to BR estimation on a 60 s long acquisition are provided in Fig. 16, which illustrates: a) the spectrograms employed for BR estimation and the corresponding BR estimates generated by the AD and by the MCPG method (see Figs. 16a and 16b, respectively); b) the probability map produced by the VSEADA (see Fig. 16c) in the frequency range of typical respiration rates and the BR estimate it produces, and; c) the BR estimate provided by our reference sensor. These results lead to the conclusion that, in the considered case, the BR estimates generated by all the algorithms follow closely the trajectory describing the true evolution of BR over time. This is due to the fact that the BR contribution to the useful component of the received signal is characterised by a high SNR; this makes radar-based estimation of this vital sign easy. Different considerations can be made for the HR estimates generated by the considered three methods in the same acquisition. These results are provided in Fig. 17 for the same acquisition processed to generate the numerical results shown in Fig. 16. More precisely, in the new figure we show: a) the spectrograms employed for HR estimation and the HR estimates generated by the AD method and by the MCPG method (see Figs. 17a and 17b, respectively); b) the probability map produced by the VSEADA (see Fig. 17c) in the frequency range of typical HRs and the HR estimate it produces, and; c) the HR estimate provided by our reference sensor. As already pointed out in Sec. III, the SNR characterizing the contribution of heart displacements to the useful component of the received signal is significantly lower than that of the counterpart due to respiration. This may lead to large estimation errors in the case of the AD and the MCPG method. The VSEADA, instead, performs appreciably better thanks to its filtering procedure that suppresses unwanted spectral components.

D. STATISTICAL ANALYSIS

A visual representation of the correlation between the VSEADA estimates and the measurements provided by the reference sensor for the whole dataset acquired under NAC is provided in Fig. 18, where scatter plots for the BR and HR are illustrated (see Figs. 18a and 18b, respectively). From these

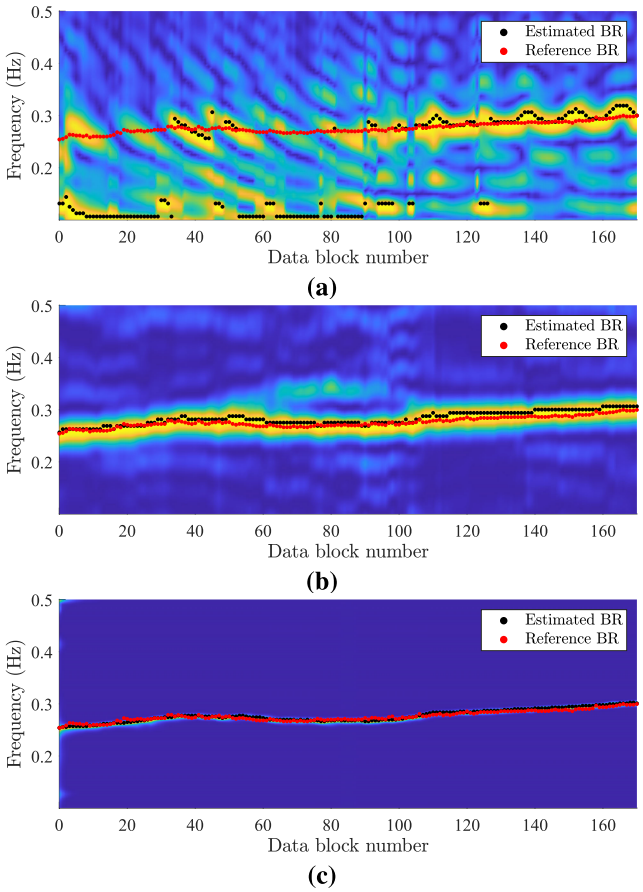

FIGURE 16. Breath rate ground truth (red dots) and estimates (black dots) for: (a) the AD method; (b) the MCPG method; (c) the VSEADA. A single acquisition from the dataset acquired under NAC is considered.

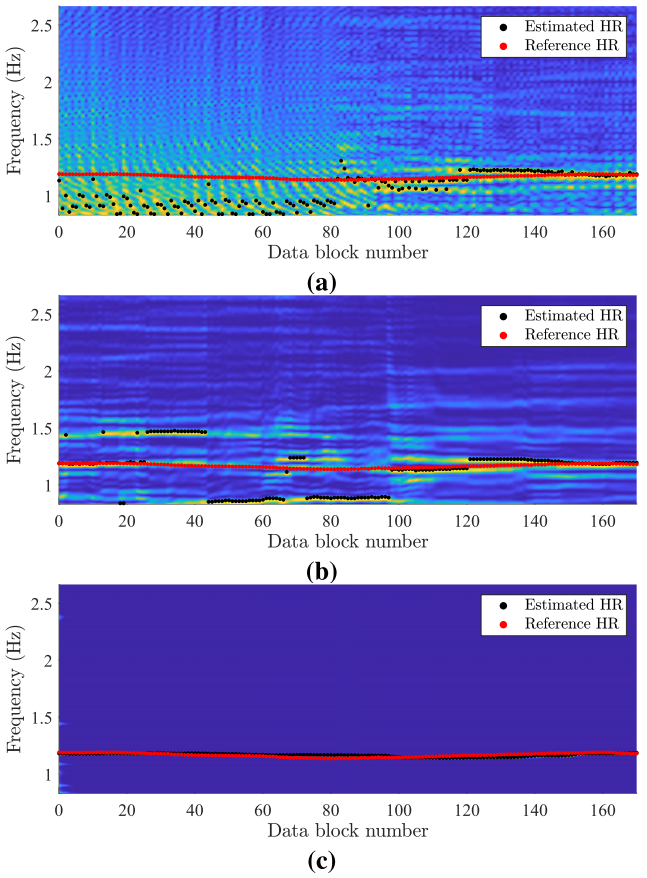

FIGURE 17. Heart rate ground truth (red dots) and estimates (black dots) versus time for: (a) the AD method; (b) the MCPG method; (c) the VSEADA. The same acquisition as Fig. 16 is considered.

results it can be inferred that most of the VSEADA estimates fall in the region delimited by the straight lines $y = x \pm 3$; therefore, a good overall accuracy is achieved, even if some outliers are visible. This behaviour confirms what has been already observed in Subsection V-B about the large PAE. Note also that the population of volunteers involved in the generation of our dataset includes subjects having basal HRs and BRs that range from 50 to 80 *beats per minute* (bpm), and from 6 and 23 acts/min, respectively.

Two non-parametric tests, namely the *Wilcoxon signed-rank test* [50, Sec 3.1] and the evaluation of the *Spearman rank correlation coefficient* [50, Sec 8.5], have been performed to assess some essential statistical properties of our dataset.[19] In particular, the first test has been run to verify the null hypothesis, i.e. the fact that the *estimation error* (i.e., the difference between the VSEADA estimate and the associated measurement provided by the reference sensor) follows a distribution with zero median [50, Sec 3.1]. This test yielded p-values equal to $1.6 \cdot 10^{-11}$ and $2.67 \cdot 10^{-22}$ for BR and HR, respectively. For this reason, the mean of the estimation error has been evaluated for both BR and HR over the whole NAC dataset. We have found that this quantity is equal to -0.33 acts/min and -0.85 bpm for BR and HR, respectively. Consequently, in both cases, the VSEADA tends to underestimate vital parameters. The second test, instead, has been run to assess the strength and direction of association between the VSEADA estimates and the corresponding reference measurements through the evaluation of the *Spearman rank correlation coefficient* r. This test, run over the NAC dataset, has resulted in a p-value approximately equal to zero for both HR and BR and a value of r equal to 0.80 and 0.93 for BR and HR, respectively. These results lead to the conclusion that the VSEADA estimates closely follow the pattern of the reference measurements.

[19]The `corr` and `signrank` Matlab functions have been adopted to compute the Spearman correlation coefficient and the Wilcoxon signed-rank, respectively.

E. DISCUSSION

To date, various radar-based VSM systems have been proposed in the technical literature and extensively tested in various real-world scenarios. Despite this, the available commercial products suffer from various limitations; in particular, they exhibit a strong sensitivity to body movements.

Various methods for mitigating the impact of RBMs can be found in the technical literature; however, none of them can be considered as a comprehensive solution. The VSEADA is able to mitigate small RBMs by leveraging the memory from previous estimates through an innovative filtering technique

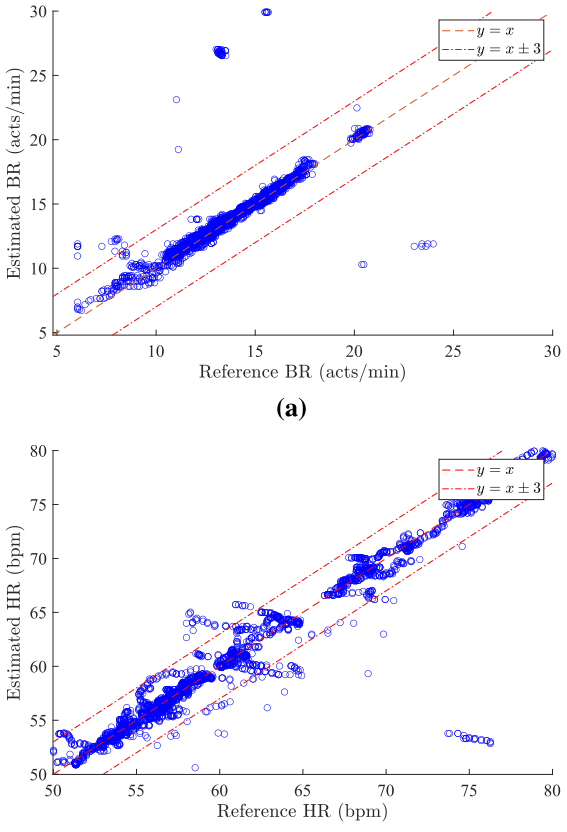

FIGURE 18. Scatter plots of the generated VSEADA estimates versus the associated reference measurements; the whole available dataset acquired under NAC for (a) BR and (b) HR is considered.

(see Section III). Our numerical results evidence that our VSM system is able to provide accurate estimates for individuals sitting at various distances from the employed radar devices, while breathing normally. These features make our system robust enough for all real-world applications in which the subject remains still, such as during medical exams like *computed tomography* or *magnetic resonance imaging*. However, our system is not suitable for scenarios involving moving subjects, such as people walking, talking, or driving.

Furthermore, various technical solutions rely on expensive devices and computationally intensive algorithms [17]. In contrast, our VSM system can run on embedded hardware and employs low-cost radar devices with a simple architecture, while maintaining sufficient accuracy and robustness. We believe that this paves the way for the development of new commercial products that can really compete with established technologies like ECG or PPG.

Radar-based VSM systems can be used not only for estimating average HR and BR, but, as emerged from recent research activities, for detecting pathological conditions such as *arrhythmias*, *fibrillations*, and *epileptic seizures*. These applications often require the estimation of instantaneous HR, defined as the inverse of the time interval between successive heartbeats. To the best of our knowledge, only few deterministic algorithms for the estimation of instantaneous HR are available in the literature, but their use for the detection of the above mentioned cardiac conditions has not been investigated yet.

VI. CONCLUSION

In this manuscript, a novel algorithm for apnea detection and the simultaneous estimation of BR and HR has been illustrated. This algorithm, dubbed VSEADA, has the following relevant features: a) it exploits a novel selection combining strategy to benefit from the spatial diversity made available by multiple SIMO radar; b) it employs a novel filtering method to identify relevant spectral components; c) it benefits from the presence of the second order harmonic of heart in HR estimation, and; d) it includes a novel apnea detection. Our numerical results, referring to two commercially available low-cost SIMO radar devices operating at 24 GHz, evidence that the VSEADA significantly outperforms the AD and CPG methods at the price of a higher computational effort. Our ongoing research activities focus on evaluating the accuracy of our VSM system on a larger group of volunteers (over 150), and on developing innovating methods for RBM mitigation and for the estimation of the instantaneous HR.

APPENDIX A
RANGE COMPRESSION AND TARGET SELECTION DETAILS

In this appendix, the model (21) is derived. To begin, the RHS of (14) is substituted in that of (18); this produces, for any RX antenna (i.e., for any $v \in \{0, 1, .., N_{\mathrm{RX}} - 1\}$), the two-dimensional complex sequence $\{X^{(v)}[l, n]\}$, where

$$X^{(v)}[l,n] = \frac{b^{(v)}}{N_0}\exp(j\psi^{(v)}[n]) \cdot \sum_{k=0}^{N-1}\exp(j2\pi\frac{k}{N_0}(N_0 f_{\mathrm{n}} T_{\mathrm{s}} - l)) + w_{\mathrm{R}}^{(v)}[l,n], \tag{79}$$

with $l = 0, 1, \ldots, N_0 - 1$ and $n = 0, 1, \ldots, N_{\mathrm{F}} - 1$; here,

$$w_{\mathrm{R}}^{(v)}[n,l] \triangleq \sum_{k=0}^{N-1} w_s^{(v)}[k,n]\exp(-j2\pi kl/N_0) \tag{80}$$

represents the noise contribution. If the SNR is high, the target detection strategy (20) is likely to select, for a given n, the value of l (denoted $\hat{l}^{(v)}[n]$) closer to $N_0 f_{\mathrm{n}} T_{\mathrm{s}}$, so that[20]

$$\frac{\hat{l}^{(v)}[n]}{N_0} \approx f_{\mathrm{n}} T_{\mathrm{s}}. \tag{81}$$

Then, from (79) it is easily inferred that

$$X^{(v)}[\hat{l}^{(v)}[n], n] \approx b^{(v)}\exp(j\psi^{(v)}[n]) + w_{\mathrm{R}}^{(v)}[n], \tag{82}$$

where

$$w_{\mathrm{R}}^{(v)}[n] \triangleq w_{\mathrm{R}}^{(v)}[\hat{l}^{(v)}[n], n]. \tag{83}$$

This proves (21).

[20]The accuracy of the following approximation improves as the FFT order (N_0) gets larger.

APPENDIX B
ANALYSIS OF THE PHASE GRADIENT

In this appendix, the spectral content of the sequence $\{s_p^{(v)}[n]\}$, whose nth element is defined by (21), is analysed under the assumptions that: a) this sequence conveys the displacement information originating from a single point target, and; b) the target displacement is expressed by (3)-(5). For simplicity, in all the following equations, the dependence on the block index p and the RX antenna index v is omitted (e.g., $s_p^{(v)}[n]$ is denoted $s[n]$) and the contribution of noise is neglected.

To begin, let us substitute (4)-(5) in the RHS of (3) and, then, the resulting expression of the target displacement in the RHS of (22) evaluated for $t = nT_F$; this yields

$$\psi[n] = \frac{4\pi}{\lambda}\left[R_0 + \frac{\delta_{b,M}}{2}\left(1 - \cos(\omega_b n T_F)\right) + \delta_{h,M}\cos(\omega_h n T_F)\right]. \tag{84}$$

Substituting the RHS of the last formula in that of (21) gives

$$s[n] = c\exp\left\{j\frac{4\pi}{\lambda}\left(-\frac{\delta_{b,M}}{2}\cos(\omega_b n T_F) + \delta_{h,M}\cos(\omega_h n T_F)\right)\right\}, \tag{85}$$

with $n = 0, 1, \ldots, N_B - 1$; here,

$$c \triangleq b\exp\left\{j4\pi\left(\frac{R_0 + \delta_{b,M}/2}{\lambda}\right)\right\} \tag{86}$$

and b is defined by (15); note that the parameter c is independent of the frame index n. Based on the *Jacobi-Anger expansion* [51], [52], [53], [54], (85) can be easily put in the form

$$\begin{aligned} s[n] &= c\sum_{m=-\infty}^{+\infty} j^m J_m\left(-\frac{2\pi\delta_{b,M}}{\lambda}\right)\exp(jm\omega_b n T_F) \\ &\cdot \sum_{u=-\infty}^{+\infty} j^u J_u\left(\frac{4\pi\delta_{h,M}}{\lambda}\right)\exp(ju\omega_h n T_F) \\ &= c\left\{C_{0,0} + 2js_I[n] + 2s_R[n]\right\}, \end{aligned} \tag{87}$$

where $s_I[n]$ and $s_R[n]$ are defined by (88) and (89), as shown at the bottom of the next page, respectively, and

$$C_{x,y} \triangleq J_x\left(-\frac{2\pi\delta_{b,M}}{\lambda}\right)J_y\left(\frac{4\pi\delta_{h,M}}{\lambda}\right) \tag{90}$$

for any x and y.

From (87)-(90) it can be inferred that the amplitudes of the breath and heart harmonics and those of the intermodulation components contained in the sequence $\{s[n]\}$ are proportional to c (86) and depend on the values of the coefficients $\{J_x(-2\pi\delta_{b,M}/\lambda)\}$ and $\{J_y(4\pi\delta_{h,M}/\lambda)\}$. Based on these mathematical results, if we assume that $f_c = 24$ GHz (i.e., $\lambda = 12.5$ mm), $\delta_{h,M} = 0.45$ mm and $\delta_{b,M} \in [8, 24]$ mm (see Sec. II), it can be shown that the FHs of both heart and respiration do not represent the dominant spectral components, since some of their HOHs exhibit a larger amplitude (see also [18]). This is exemplified by Fig. 19a, in which the amplitude of multiple harmonics of heart and respiration is illustrated; note that the coefficients $C_{0,1}$ and $C_{1,0}$ are associated to the FHs of heart and breath, respectively. These considerations lead to the conclusion that the use of the periodogram method for estimating BR and HR on the basis of the amplitude spectrum of $\{s[n]\}$ (as accomplished by the AD method; see Subsection IV-A) may lead to erroneous estimates of vital signs. Recent work illustrated in [18] has evidenced the benefits that, in the estimation of BR, originate from replacing the complex sequence $\{s[n]; n = 0, 1, .., N_B - 1\}$ with the real sequence $\{g[n]; n = 0, 1, .., N_B - \Delta n - 1\}$, where

$$g[n] \triangleq \Im\{f[n]\} \tag{91}$$

and

$$f[n] \triangleq s[n]\cdot(s[n+\Delta n])^*, \tag{92}$$

represents the nth element of the PG sequence (see (29)). If the model (87) is adopted for $s[n]$, $f[n]$ (92) can be easily put in the form

$$f[n] = |c|^2 \cdot y_b[n]\cdot y_h[n], \tag{93}$$

where

$$y_b[n] \triangleq \exp\left\{-j\frac{4\pi\delta_{b,M}}{\lambda}\sin\left(\frac{\omega_b\Delta n T_F}{2}\right)\cdot\sin\left(\omega_b(n+\frac{\Delta n}{2})T_F\right)\right\} \tag{94}$$

and

$$y_h[n] \triangleq \exp\left\{j\frac{8\pi\delta_{h,M}}{\lambda}\sin\left(\frac{\omega_h\Delta n T_F}{2}\right)\cdot\sin\left(\omega_h(n+\frac{\Delta n}{2})T_F\right)\right\} \tag{95}$$

for $n = 0, 1, \ldots, N_B - \Delta n - 1$; note that the factors $y_b[n]$ and $y_h[n]$ represent the contributions due to breath and heart, respectively. An alternative representation of $f[n]$ (93) can be obtained by applying the *Jacobi-Anger expansion* to both $y_b[n]$ (94) and $y_h[n]$ (95); this gives $f[n]$ (96), as shown at the bottom of the next page, where $f_I[n]$ and $f_Q[n]$ are defined as (97) and (98), shown at the bottom of the next page, respectively, and

$$D_{x,y} \triangleq J_x\left(-\frac{4\pi\delta_{b,M}}{\lambda}\sin\left(\frac{\omega_b\Delta n T_F}{2}\right)\right) J_y\left(\frac{8\pi\delta_{h,M}}{\lambda}\sin\left(\frac{\omega_h\Delta n T_F}{2}\right)\right) \tag{99}$$

for any x and y. Eq. (96) implies that the amplitudes of breath and heart harmonics and those of the intermodulation components contained in the sequence $\{f[n]\}$ are proportional to the scale factor $|c|^2$ (99) and to the values of the coefficients $\{J_x(-4\pi\delta_{b,M}/\lambda \cdot \sin(\omega_b\Delta n T_F/2))\}$ and $\{J_y(8\pi\delta_{h,M}/\lambda)\cdot\sin(\omega_h\Delta n T_F/2))\}$. Comparing (99) with (90) evidences that the uses of the PG operation (92) entail a reduction of the argument of Bessel functions associated with breath and

heart according to the scale factors $\sin(\omega_b \Delta n T_F/2)/2$ and $\sin(\omega_h \Delta n T_F/2)/2$, respectively. In general, this results in a reduction of the amplitude of the HOHs and makes the FH of both heart and breath significantly stronger than HOHs and intermodulation products. This effect is exemplified by Fig. 19b, in which the amplitudes of multiple harmonics of heart and respiration for $\delta_{b,M} \in [8, 24]$ mm and $\delta_{h,M} = 0.45$ mm are shown; note that the amplitude of the DC (due to the presence of the term $D_{0,0}$ in (96)) is significant. Further benefits are provided by the extraction of the imaginary part of $f[n]$, i.e. by the evaluation of $g[n]$ (91). In fact, substituting (96) in the RHS of (91) yields

$$g[n] = 2|c|^2 f_I[n], \tag{100}$$

where $f_I[n]$ is defined as in (97). The last result leads to the conclusion that the sequence $\{g[n]\}$ does not contain even-order harmonics, intermodulation products, and DC. This is exemplified by Fig. 19c, where the amplitudes of multiple harmonics of heart and respiration are shown for $\delta_{b,M} \in [8, 24]$ mm and $\delta_{h,M} = 0.4$ mm. These results evidence that: a) the breath FH is stronger than any other spectral component; b) the heart FH is stronger than any intermodulation product and any other HOH of heart and breath. These results hold for both the sequences $\{f[n]\}$ and $\{g[n]\}$, if the presence of DC in the first sequence is neglected. Unluckily, these results, obtained through a mathematical approach, do not fully agree with our experimental results (see Section V). In fact, our measurements have evidenced that the spectrum of $\{g[n]\}$ contains the second harmonic of heart and that this component is often stronger than the FH. We believe that the mismatch between our mathematical results and their experimental counterpart originates from the approximated model for chest displacement adopted in our analysis (see (3) and (5)).

$$\begin{aligned} s_I[n] \triangleq & \sum_{m=0}^{+\infty} (-1)^m \left\{ C_{0,2m+1} \cos((2m+1)\omega_h n T_F) + C_{2m+1,0} \cos((2m+1)\omega_b n T_F) \right\} \\ & + \sum_{m=0}^{+\infty} \sum_{u=1}^{+\infty} (-1)^{m+u} \left\{ C_{2m+1,2u} \left[\cos(((2m+1)\omega_b - 2u\omega_h) n T_F) + \cos((2u\omega_h - (2m+1)\omega_b) n T_F) \right] \right. \\ & \left. + C_{2m+2,2u-1} \left[\cos(((2m+2)\omega_b - (2u-1)\omega_h) n T_F) + \cos(((2u-1)\omega_h - (2m+2)\omega_b) n T_F) \right] \right\} \end{aligned} \tag{88}$$

$$\begin{aligned} s_R[n] \triangleq & \sum_{m=1}^{+\infty} (-1)^m \left\{ C_{0,2m} \cos(2m\omega_h n T_F) + C_{2m,0} \cos(2m\omega_b n T_F) \right\} + \sum_{m=1}^{+\infty} \sum_{u=1}^{+\infty} (-1)^{m+u} \left\{ C_{2m,2u} \left[\cos((2m\omega_b - 2u\omega_h) n T_F) \right. \right. \\ & \left. + \cos((2u\omega_h - 2m\omega_b) n T_F) \right] - C_{2m-1,2u-1} \left[\cos(((2m-1)\omega_b - (2u-1)\omega_h) n T_F) \right. \\ & \left. \left. + \cos(((2u-1)\omega_h - (2m-1)\omega_b) n T_F) \right] \right\} \end{aligned} \tag{89}$$

$$\begin{aligned} f[n] &= |c|^2 \sum_{m=-\infty}^{+\infty} j^m J_m\left(-\frac{4\pi \delta_{b,M}}{\lambda} \sin\left(\frac{\omega_b \Delta n T_F}{2} \right) \right) \exp\left\{ jm\omega_b \left(n + \frac{\Delta n}{2} \right) T_F \right\} \\ &\quad \cdot \sum_{u=-\infty}^{+\infty} j^u J_u\left(\frac{8\pi \delta_{h,M}}{\lambda} \sin\left(\frac{\omega_h \Delta n T_F}{2} \right) \right) \exp\left\{ ju\omega_h \left(n + \frac{\Delta n}{2} \right) T_F \right\} \\ &= |c|^2 \left\{ D_{0,0} + 2jf_I[n] + 2f_R[n] \right\} \end{aligned} \tag{96}$$

$$\begin{aligned} f_I[n] \triangleq & \sum_{m=0}^{+\infty} \left\{ D_{0,2m+1} \cos\left((2m+1)\omega_h \left(n + \frac{\Delta n}{2} \right) T_F \right) - D_{2m+1,0} \cos\left((2m+1)\omega_b \left(n + \frac{\Delta n}{2} \right) T_F \right) \right\} \\ & + \sum_{m=0}^{+\infty} \sum_{u=1}^{+\infty} \left\{ - D_{2m+1,2u} \left[\sin\left(((2m+1)\omega_b - 2u\omega_h) \cdot \left(n + \frac{\Delta n}{2} \right) T_F \right) + \sin\left((2u\omega_h - (2m+1)\omega_b) \cdot \left(n + \frac{\Delta n}{2} \right) T_F \right) \right] \right. \\ & \left. + D_{2m+2,2u-1} \left[\cos\left(((2m+2)\omega_b - (2u-1)\omega_h) \cdot \left(n + \frac{\Delta n}{2} \right) T_F \right) + \cos\left(((2u-1)\omega_h - (2m+2)\omega_b) \cdot \left(n + \frac{\Delta n}{2} \right) T_F \right) \right] \right\} \end{aligned} \tag{97}$$

$$\begin{aligned} f_R[n] \triangleq & \sum_{m=1}^{+\infty} \left[D_{0,2m} \cos\left(2m\omega_h \left(n + \frac{\Delta n}{2} \right) T_F \right) + D_{2m,0} \cos\left(2m\omega_b \left(n + \frac{\Delta n}{2} \right) T_F \right) \right] + \sum_{m=0}^{+\infty} \sum_{u=0}^{+\infty} \left\{ D_{2m+1,2u+1} \right. \\ & \left. \cdot \left[\sin\left(((2m+1)\omega_b - (2u+1)\omega_h) \cdot \left(n + \frac{\Delta n}{2} \right) T_F \right) + \sin\left(((2u+1)\omega_h - (2m+1)\omega_b) \cdot \left(n + \frac{\Delta n}{2} \right) T_F \right) \right] \right\} \end{aligned} \tag{98}$$

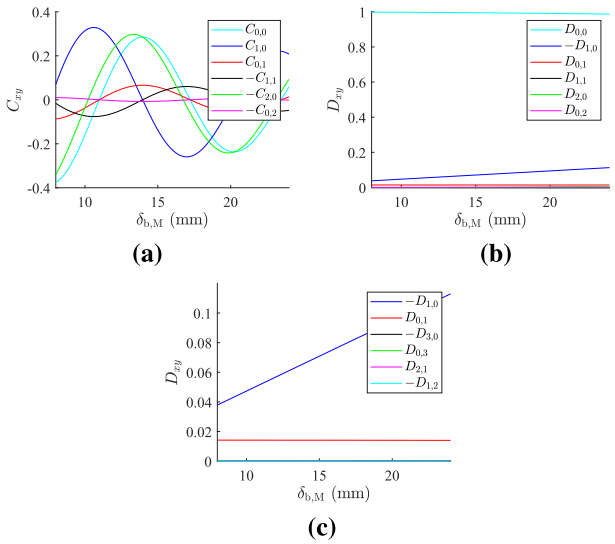

FIGURE 19. Representation of the amplitudes, versus $\delta_{b,M}$, of multiple sinusoidal components of the following sequences: (a) $\{s[n]\}$ (87); (b) $\{f[n]\}$ (96); (c) $\{g[n]\}$ (100). In all cases, $f_c = 24$ GHz, $T_F = 0.1$ s, $f_b = 0.3$ Hz, $f_h = 1$ Hz, $\delta_{h,M} = 0.45$ mm and $\Delta[n] = 1$ are assumed.

APPENDIX C
COMPUTATIONAL COMPLEXITY

In this appendix, the computational complexities, in terms of *floating-point operations* (flops), of the three VSM algorithms described in Sections III-IV are derived. To begin, it is useful to note that computational complexity $\mathcal{C}_{\text{alg}}$ of each algorithm can be expressed as

$$\mathcal{C}_{\text{alg}} \triangleq \mathcal{C}_{\text{alg}}^{(\text{pre})} + \mathcal{C}_{\text{alg}}^{(\text{main})}, \tag{101}$$

where:

a) $\mathcal{C}_{\text{alg}}^{(\text{pre})}$ represents the cost of the *pre-processing steps* involving N_F consecutive superframes. In the VSEADA, these include coherent combining and target detection (see (13) and (19)), whereas beamforming is also taken into account in the other methods.

b) $\mathcal{C}_{\text{alg}}^{(\text{main})}$ represents the cost of the *main processing steps for a single data block*, which encompasses N_B consecutive superframes.

c) The symbol 'alg' denotes the considered algorithm (VSEADA, AD, or MCPG).

The general criteria adopted in assessing $\mathcal{C}_{\text{alg}}^{(\text{pre})}$ and $\mathcal{C}_{\text{alg}}^{(\text{main})}$ are the same as those illustrated in [55] and can be summarised as follows:

- $2d$ flops are required to compute the element-wise sum $\mathbf{u}_c + \mathbf{v}_c$ of two d-dimensional complex vectors;
- $6d$ flops are required to compute the element-wise product $\mathbf{u}_c \cdot \mathbf{v}_c$ of two d-dimensional complex vectors;
- d flops are required to find the maximum element of a vector $\mathbf{v} \in \mathbb{R}^d$;
- $d \log_2 d$ flops are required to compute an order d FFT.

Detailed expressions of $\mathcal{C}_{\text{alg}}^{(\text{pre})}$ and $\mathcal{C}_{\text{alg}}^{(\text{main})}$ are provided below for each method.

VSEADA - This method exploits multiple (say, N_D) SIMO radars (see Sec. II) and processes $\tilde{N}_{RX}$ received signals for the estimation of vital signs: moreover, beamforming is not exploited. Its computational cost $\mathcal{C}_{\text{VSEADA}}^{(\text{pre})}$ is evaluated as

$$\mathcal{C}_{\text{VSEADA}}^{(\text{pre})} = \left(\mathcal{C}_x + \mathcal{C}_X + \mathcal{C}_{\hat{l}}\right) N_F \tilde{N}_{RX} \tag{102}$$

where: a) $\mathcal{C}_x = 2N(N_C - 1)$ is the contribution due to the computation of the sequence $\{x^{(v)}[k,n]\}$ (13); b) $\mathcal{C}_X = N_0 \log_2 N_0$ is the contribution due to the computation of the matrix $\mathbf{X}^{(v)}$ (17); c) $\mathcal{C}_{\hat{l}} = 6(l_{\max} - l_{\min})$ is the contribution due to the computation of the sequence $\{\hat{l}^{(v)}[n]\}$ (19).

The cost $\mathcal{C}_{\text{VSEADA}}^{(\text{main})}$, instead, is evaluated for a single data block as

$$\mathcal{C}_{\text{VSEADA}}^{(\text{main})} = \mathcal{C}_{f_0} + \mathcal{C}_{\text{SFEC}} + \mathcal{C}_Q + \mathcal{C}_{\text{TU}} + \mathcal{C}_{\text{MU}} + \mathcal{C}_{\hat{n}} \tag{103}$$

where: a) $\mathcal{C}_{f_0} = 6(N_B - \Delta n)\tilde{N}_{RX}$ is the contribution due to the computation of $\{f_{0,p}^{(v)}[n]\}$ on the basis of (29); b) $\mathcal{C}_{\text{SFEC}} = [N_0' \log_2 N_0' + K_{\text{SFEC}} N_{\text{SFEC}} I^2 (M_h + M_b)]\tilde{N}_{RX}$ is the contribution due to the computation of $\{(\mathbf{g}_{0,p}^{(v)}, \mathbf{g}_{1,p}^{(v)}, \mathbf{g}_{2,p}^{(v)})\}$ (30) and to the execution of the SFEC algorithm[21] (N_{SFEC} is the number of refinement iterations, $K_{\text{SFEC}} = 2/3$ and $I = 7$); c) $\mathcal{C}_Q = [6(M_h + M_b) - 1]\tilde{N}_{RX}$ is the contribution due to the computation of $\{\mathbf{a}_x^{(v)}[p]\}$ (36) and $\{Q^{(v)}\}$ (37); d) $\mathcal{C}_{\text{TU}} = (\hat{n}_{\max}^{(h)} - \hat{n}_{\min}^{(h)})N_h + (\hat{n}_{\max}^{(b)} - \hat{n}_{\min}^{(b)})N_b$ is the overall contribution due to the computation of $\{\hat{\alpha}_m^{(h)}[p]\}$ (42) and $\{\hat{\alpha}_m^{(b)}[p]\}$; e) $\mathcal{C}_{\text{MU}} = \mathcal{C}_f + 3(N_h + N_b)$ is the overall contribution due to the computation of $\{\alpha_n^{(h)}[p]\}$ and $\{\alpha_n^{(b)}[p]\}$ (47); here, $\mathcal{C}_f = 10(N_h \bar{M}_h + N_b \bar{M}_b)$ is the overall contribution due to the computation of $f_p^{(h)}$ (49) and $f_p^{(b)}$ (64); f) $\mathcal{C}_{\hat{n}} = 3(N_h + N_b)$ is the contribution due to the computation of $\hat{n}^{(h)}[p]$ and $\hat{n}^{(b)}[p]$ (see (54)). Based on the last mathematical results, (101), (102) and (103), the overall complexity of the VSEADA can be expressed as

$$\begin{aligned}\mathcal{C}_{\text{VSEADA}} = &\Big\{\big[2N(N_C - 1) + N_0 \log_2 N_0 \\ &+ 6(l_{\max} - l_{\min})\big] N_F + 6(N_B - \Delta n) + N_0' \log_2 N_0' \\ &+ (M_h + M_b)(K_{\text{SFEC}} N_{\text{SFEC}} I^2 + 6) - 1\Big\} \tilde{N}_{RX} \\ &+ \left(\hat{n}_{\max}^{(h)} - \hat{n}_{\min}^{(h)} + 10\bar{M}_h + 6\right) N_h \\ &+ \left(\hat{n}_{\max}^{(b)} - \hat{n}_{\min}^{(b)} + 10\bar{M}_b + 6\right) N_b. \end{aligned} \tag{104}$$

AD - This method exploits a single SIMO radar (see Sec. II) and processes N_{RX} received signals for the estimation of vital signs. Its computational cost $\mathcal{C}_{\text{AD}}^{(\text{pre})}$ is evaluated as

$$\mathcal{C}_{\text{AD}}^{(\text{pre})} = \mathcal{C}_{\text{BF}} + \left(\mathcal{C}_x + \mathcal{C}_X + \mathcal{C}_{\hat{l}}\right) N_F N_{RX} \tag{105}$$

where: a) $\mathcal{C}_{\text{BF}} = 2(N_{RX} - 1)N_F N$ is the contribution due to beamforming (performed by coherently summing the contributions of the available RX antennas); b) $\mathcal{C}_x$, $\mathcal{C}_X$, and $\mathcal{C}_{\hat{l}}$ are identical to those evaluated for the VSEADA.

The cost $\mathcal{C}_{\text{AD}}^{(\text{main})}$, instead, is evaluated as

$$\mathcal{C}_{\text{AD}}^{(\text{main})} = \mathcal{C}_{\phi'} + \mathcal{C}_{\text{FFT}} + \mathcal{C}_{\text{AD}}^{(\text{est})} \tag{106}$$

[21] A complete derivation of the computational cost of the SFEC can be found in [21].

where: a) $\mathcal{C}_{\phi'} = 4N_{\mathrm{B}}$ is the contribution due to the computation of $\{\phi'[n]\}$ (68)-(69); b) $\mathcal{C}_{\mathrm{FFT}} = N'_0 \log_2 N'_0$ is the contribution due to the computation of the spectral sequence $\{Y_{\mathrm{AD}}[n]\}$; c) $\mathcal{C}_{\mathrm{AD}}^{(\mathrm{est})} = 6\left(h_{\max}^{(\mathrm{h})} - h_{\min}^{(\mathrm{h})} + h_{\max}^{(\mathrm{b})} - h_{\min}^{(\mathrm{b})}\right) + 2$ is the contribution due to the computation of $\hat{f}_{\mathrm{b,AD}}$ and $\hat{f}_{\mathrm{h,AD}}$ according to (70)-(73). Based on the last results, (101), (105) and (106), the overall complexity of the AD method can be expressed as

$$\begin{aligned}\mathcal{C}_{\mathrm{AD}} = {} & \{[2N(N_{\mathrm{C}}-1)+2N]N_{\mathrm{RX}} - 2N + N_0 \log_2 N_0 \\ & + 6(l_{\max} - l_{\min})\}N_{\mathrm{F}} + 4N_{\mathrm{B}} + N'_0 \log_2 N'_0 \\ & + 6\left(h_{\max}^{(\mathrm{h})} - h_{\min}^{(\mathrm{h})} + h_{\max}^{(\mathrm{b})} - h_{\min}^{(\mathrm{b})}\right) + 2. \end{aligned} \tag{107}$$

MCPG - Similarly to the AD, this method exploits a single SIMO radar (see Sec. II) and processes N_{RX} received signals. The cost $\mathcal{C}_{\mathrm{MCPG}}^{(\mathrm{pre})}$ is identical to that of the corresponding term evaluated for the AD method; hence,

$$\mathcal{C}_{\mathrm{MCPG}}^{(\mathrm{pre})} = \mathcal{C}_{\mathrm{AD}}^{(\mathrm{pre})}. \tag{108}$$

The cost of $\mathcal{C}_{\mathrm{MCPG}}^{(\mathrm{main})}$, instead, is evaluated as

$$\mathcal{C}_{\mathrm{MCPG}}^{(\mathrm{main})} = \left(\mathcal{C}_f + \mathcal{C}_{G_l}\right) L + \mathcal{C}_G + \mathcal{C}_{\mathrm{MCPG}}^{(\mathrm{est})} \tag{109}$$

where: a) $\mathcal{C}_f = 6(N_{\mathrm{B}} - \Delta n)$ is the contribution due to the computation of the sequence $\mathbf{g}_l$ (74); b) $\mathcal{C}_{G_l} = N'_0 \log_2 N'_0$ is the contribution due to the computation of $\mathbf{G}_l$ (77); c) $\mathcal{C}_G = (L-1)N'_0$ is the contribution due to the computation of $\{G_{\mathrm{MCPG}}[m]\}$ (see (78)); d) $\mathcal{C}_{\mathrm{MCPG}}^{(\mathrm{est})}$, the contribution due to the computation of $\hat{f}_{\mathrm{b,MCPG}}$ and $\hat{f}_{\mathrm{h,MCPG}}$, is identical to that of the corresponding term evaluated for the AD method. Based on the last results, (101), (108) and (109), it can be shown that

$$\begin{aligned}\mathcal{C}_{\mathrm{MCPG}} = {} & \{[2N(N_{\mathrm{C}}-1)+2N]N_{\mathrm{RX}} - 2N + N_0 \log_2 N_0 \\ & + 6(l_{\max} - l_{\min})\}N_{\mathrm{F}} + \left[6(N_{\mathrm{B}} - \Delta n) + N'_0 \log_2 N'_0\right] L \\ & + (L-1)N'_0 + 6\left(h_{\max}^{(\mathrm{h})} - h_{\min}^{(\mathrm{h})} + h_{\max}^{(\mathrm{b})} - h_{\min}^{(\mathrm{b})}\right) + 2. \end{aligned} \tag{110}$$

REFERENCES

[1] M. Kebe, R. Gadhafi, B. Mohammad, M. Sanduleanu, H. Saleh, and M. Al-Qutayri, "Human vital signs detection methods and potential using radars: A review," *Sensors*, vol. 20, no. 5, p. 1454, Mar. 2020.

[2] Y. Wu, H. Ni, C. Mao, J. Han, and W. Xu, "Non-intrusive human vital sign detection using mmWave sensing technologies: A review," *ACM Trans. Sensor Netw.*, vol. 20, no. 1, pp. 1–36, Nov. 2023.

[3] M. Liebetruth, K. Kehe, D. Steinritz, and S. Sammito, "Systematic literature review regarding heart rate and respiratory rate measurement by means of radar technology," *Sensors*, vol. 24, no. 3, p. 1003, Feb. 2024.

[4] G. Paterniani, D. Sgreccia, A. Davoli, G. Guerzoni, P. Di Viesti, A. C. Valenti, M. Vitolo, G. M. Vitetta, and G. Boriani, "Radar-based monitoring of vital signs: A tutorial overview," *Proc. IEEE*, vol. 111, no. 3, pp. 277–317, Mar. 2023.

[5] C. Will, K. Shi, S. Schellenberger, T. Steigleder, F. Michler, J. Fuchs, R. Weigel, C. Ostgathe, and A. Koelpin, "Radar-based heart sound detection," *Sci. Rep.*, vol. 8, no. 1, p. 11551, Jul. 2018.

[6] L. Ren, S. Nahar, A. E. Fathy, T. Phan, N. Tran, and O. Kilic, "Investigation of vital signs monitoring errors due to subject's orientation, clothing and distance from a SFCW radar," in *Proc. IEEE Int. Symp. Antennas Propag. (APSURSI)*, Jun. 2016, pp. 1171–1172.

[7] B.-K. Park, O. Boric-Lubecke, and V. M. Lubecke, "Arctangent demodulation with DC offset compensation in quadrature Doppler radar receiver systems," *IEEE Trans. Microw. Theory Techn.*, vol. 55, no. 5, pp. 1073–1079, May 2007.

[8] M. Nosrati and N. Tavassolian, "Accurate Doppler radar-based cardiopulmonary sensing using chest-wall acceleration," *IEEE J. Electromagn., RF Microw. Med. Biol.*, vol. 3, no. 1, pp. 41–47, Mar. 2019.

[9] C. Li and J. Lin, "Random body movement cancellation in Doppler radar vital sign detection," *IEEE Trans. Microw. Theory Techn.*, vol. 56, no. 12, pp. 3143–3152, Dec. 2008.

[10] K. Han and S. Hong, "Differential-phase radar with amplitude-compensated complex signal demodulation for vital sign detection," in *Proc. IEEE Asia–Pacific Microw. Conf. (APMC)*, Dec. 2019, pp. 1390–1392.

[11] C. Li, Y. Xiao, and J. Lin, "Experiment and spectral analysis of a low-power *Ka*-band heartbeat detector measuring from four sides of a human body," *IEEE Trans. Microw. Theory Techn.*, vol. 54, no. 12, pp. 4464–4471, Dec. 2006.

[12] I. Walterscheid and G. E. Smith, "Respiration and heartbeat monitoring using a distributed pulsed MIMO radar," in *Proc. 39th Annu. Int. Conf. IEEE Eng. Med. Biol. Soc. (EMBC)*, Jul. 2017, pp. 3449–3452.

[13] Q. Wu, Z. Mei, Z. Lai, D. Li, and D. Zhao, "A non-contact vital signs detection in a multi-channel 77 GHz LFMCW radar system," *IEEE Access*, vol. 9, pp. 49614–49628, 2021.

[14] M. Alizadeh, G. Shaker, J. C. M. D. Almeida, P. P. Morita, and S. Safavi-Naeini, "Remote monitoring of human vital signs using mm-wave FMCW radar," *IEEE Access*, vol. 7, pp. 54958–54968, 2019.

[15] A. Ahmad, J. C. Roh, D. Wang, and A. Dubey, "Vital signs monitoring of multiple people using a FMCW millimeter-wave sensor," in *Proc. IEEE Radar Conf.*, Apr. 2018, pp. 1450–1455.

[16] L. Anitori, A. de Jong, and F. Nennie, "FMCW radar for life-sign detection," in *Proc. IEEE Radar Conf.*, May 2009, pp. 1–6.

[17] Y. Zhang, R. Yang, Y. Yue, E. G. Lim, and Z. Wang, "An overview of algorithms for contactless cardiac feature extraction from radar signals: Advances and challenges," *IEEE Trans. Instrum. Meas.*, vol. 72, pp. 1–20, 2023.

[18] Q. Wu, X. Huang, Y. Chen, J. Li, and W. Zhu, "Multitarget respiration monitoring based on cumulative phase gradient approach," *IEEE Geosci. Remote Sens. Lett.*, vol. 20, pp. 1–5, 2023.

[19] V. P. Tran, A. A. Al-Jumaily, and S. M. S. Islam, "Doppler radar-based non-contact health monitoring for obstructive sleep apnea diagnosis: A comprehensive review," *Big Data Cognit. Comput.*, vol. 3, no. 1, p. 3, Jan. 2019.

[20] J. Li, Y. Chen, S. Yao, P. Li, K. Yin, and Q. Wu, "Harmonic suppression phase gradient demodulation for vital sign monitoring," *IEEE Trans. Instrum. Meas.*, vol. 73, pp. 1–16, 2024.

[21] P. Di Viesti, A. Davoli, G. Guerzoni, and G. M. Vitetta, "Novel methods for approximate maximum likelihood estimation of multiple superimposed undamped tones and their application to radar systems," *Techrxiv*, pp. 13–16, Aug. 2021.

[22] G. M. Vitetta. (2024). *Frequency Estimation Toolbox*. [Online]. Available: https://www.mathworks.com/matlabcentral/fileexchange/165131-frequency-estimation-toolbox

[23] A. Gharamohammadi, M. Pirani, A. Khajepour, and G. Shaker, "Multibin breathing pattern estimation by radar fusion for enhanced driver monitoring," *IEEE Trans. Instrum. Meas.*, vol. 73, pp. 1–12, 2024.

[24] A. Albanese, L. Cheng, M. Ursino, and N. W. Chbat, "An integrated mathematical model of the human cardiopulmonary system: Model development," *Amer. J. Physiol.-Heart Circulatory Physiol.*, vol. 310, no. 7, pp. 899–921, Apr. 2016.

[25] X. Yang, Y. Yu, H. Qian, X. Zhang, and L. Zhang, "Body orientation and vital sign measurement with IR-UWB radar network," in *Proc. 42nd Annu. Int. Conf. IEEE Eng. Med. Biol. Soc. (EMBC)*, Jul. 2020, pp. 485–488.

[26] D. Wang, S. Yoo, and S. H. Cho, "Experimental comparison of IR-UWB radar and FMCW radar for vital signs," *Sensors*, vol. 20, no. 22, p. 6695, Nov. 2020.

[27] M. Mercuri, Y.-H. Liu, I. Lorato, T. Torfs, A. Bourdoux, and C. Van Hoof, "Frequency-tracking CW Doppler radar solving small-angle approximation and null point issues in non-contact vital signs monitoring," *IEEE Trans. Biomed. Circuits Syst.*, vol. 11, no. 3, pp. 671–680, Jun. 2017.

[28] M. Zhou, Y. Liu, S. Wu, C. Wang, Z. Chen, and H. Li, "A novel scheme of high-precision heart rate detection with a mm-wave FMCW radar," *IEEE Access*, vol. 11, pp. 85118–85136, 2023.
[29] S. M. Patole, M. Torlak, D. Wang, and M. Ali, "Automotive radars: A review of signal processing techniques," *IEEE Signal Process. Mag.*, vol. 34, no. 2, pp. 22–35, Mar. 2017.
[30] A. Davoli, G. Guerzoni, and G. M. Vitetta, "Machine learning and deep learning techniques for colocated MIMO radars: A tutorial overview," *IEEE Access*, vol. 9, pp. 33704–33755, 2021.
[31] T. K. V. Dai, K. Oleksak, T. Kvelashvili, F. Foroughian, C. Bauder, P. Theilmann, A. E. Fathy, and O. Kilic, "Enhancement of remote vital sign monitoring detection accuracy using multiple-input multiple-output 77 GHz FMCW radar," *IEEE J. Electromagn., RF Microw. Med. Biol.*, vol. 6, no. 1, pp. 111–122, Mar. 2022.
[32] M. Nosrati, S. Shahsavari, S. Lee, H. Wang, and N. Tavassolian, "A concurrent dual-beam phased-array Doppler radar using MIMO beamforming techniques for short-range vital-signs monitoring," *IEEE Trans. Antennas Propag.*, vol. 67, no. 4, pp. 2390–2404, Apr. 2019.
[33] I. Walterscheid, O. Biallawons, and P. Berens, "Contactless respiration and heartbeat monitoring of multiple people using a 2-D imaging radar," in *Proc. 41st Annu. Int. Conf. IEEE Eng. Med. Biol. Soc. (EMBC)*, Jul. 2019, pp. 3720–3725.
[34] Y. Rong, A. Dutta, A. Chiriyath, and D. W. Bliss, "Motion-tolerant non-contact heart-rate measurements from radar sensor fusion," *Sensors*, vol. 21, no. 5, p. 1774, Mar. 2021.
[35] X. Zhang, X. Yang, Y. Ding, Y. Wang, J. Zhou, and L. Zhang, "Contactless simultaneous breathing and heart rate detections in physical activity using IR-UWB radars," *Sensors*, vol. 21, no. 16, p. 5503, Aug. 2021.
[36] Y. Rong, K. V. Mishra, and D. W. Bliss, "Multiple moving targets heartbeat estimation and recovery using multi-frequency radars," in *Proc. IEEE Radar Conf.*, May 2021, pp. 1–5.
[37] P. D. Viesti, A. Davoli, G. Guerzoni, and G. M. Vitetta, "Recursive algorithms for the estimation of multiple superimposed undamped tones and their application to radar systems," *IEEE Trans. Aerosp. Electron. Syst.*, vol. 59, no. 2, pp. 1834–1853, Apr. 2023.
[38] J. Selva, "ML estimation and detection of multiple frequencies through periodogram estimate refinement," *IEEE Signal Process. Lett.*, vol. 24, no. 3, pp. 249–253, Mar. 2017.
[39] B. Zhang, B. Jiang, R. Zheng, X. Zhang, J. Li, and Q. Xu, "Pi-ViMo: Physiology-inspired robust vital sign monitoring using mmWave radars," *ACM Trans. Internet Things*, vol. 4, no. 2, pp. 1–27, May 2023.
[40] B.-K. Park, S. Yamada, O. Boric-Lubecke, and V. Lubecke, "Single-channel receiver limitations in Doppler radar measurements of periodic motion," in *Proc. IEEE Radio Wireless Symp.*, Oct. 2006, pp. 99–102.
[41] S. Särkkä and L. Svensson, *Bayesian Filtering and Smoothing*, vol. 17. Cambridge, U.K.: Cambridge Univ. Press, 2023.
[42] M. Pour Ebrahim, M. Sarvi, and M. Yuce, "A Doppler radar system for sensing physiological parameters in walking and standing positions," *Sensors*, vol. 17, no. 3, p. 485, Mar. 2017.
[43] Z. Chen, Y. Liu, C. Sui, M. Zhou, and Y. Song, "A novel scheme for suppression of human motion effects in non-contact heart rate detection," *IEEE Access*, vol. 11, pp. 84241–84257, 2023.
[44] M. Scherhäufl, F. Hammer, M. Pichler-Scheder, C. Kastl, and A. Stelzer, "Radar distance measurement with Viterbi algorithm to resolve phase ambiguity," *IEEE Trans. Microw. Theory Techn.*, vol. 68, no. 9, pp. 3784–3793, Sep. 2020.
[45] C. Li and J. Lin, "Complex signal demodulation and random body movement cancellation techniques for non-contact vital sign detection," in *IEEE MTT-S Int. Microw. Symp. Dig.*, Jun. 2008, pp. 567–570.
[46] Infineon Technologies. (2024). *Demo Position2Go*. [Online]. Available: https://www.infineon.com/cms/en/product/evaluation-boards/demo-position2go/
[47] Shimmer. (2018). *Shimmer3 ECG Unit*. [Online]. Available: https://shimmersensing.com/product/shimmer3-ecg-unit-2/
[48] J. Pan and W. J. Tompkins, "A real-time QRS detection algorithm," *IEEE Trans. Biomed. Eng.*, vol. BME-32, no. 3, pp. 230–236, Mar. 1985.
[49] A. C. Guyton, *Text Book of Medical Physiology*. China, 2006.
[50] M. Hollander, D. A. Wolfe, and E. Chicken, *Nonparametric Statistical Methods*. Hoboken, NJ, USA: Wiley, 2013.
[51] D. L. Colton and R. Kress, *Inverse Acoustic and Electromagnetic Scattering Theory*, vol. 93. Berlin, Germany: Springer, 1998.
[52] A. Cuyt, V. Petersen, B. Verdonk, H. Waadeland, and W. B. Jones, *Handbook of Continued Fractions for Special Functions*. Berlin, Germany: Springer, 2008.
[53] G. N. Watson, *A Treatise on the Theory of Bessel Functions*. Cambridge, U.K.: Cambridge Univ. Press, 2012.
[54] G. B. Arfken, H. J. Weber, and F. E. Harris, *Mathematical Methods for Physicists*. Orlando, FL, USA: Academic, 2013.
[55] G. H. Golub and C. F. Van Loan, *Matrix Computations*. Baltimore, MD, USA: The Johns Hopkins Univ. Press, 2013.

ELIA VIGNOLI (Graduate Student Member, IEEE) received the bachelor's and master's degrees (cum laude) in electronics engineering from the University of Modena and Reggio Emilia, in 2020 and 2022, respectively, where he is currently pursuing the Ph.D. degree in information and communication technologies. His main research interests include mm-wave radars for vital signs monitoring, with a particular emphasis on the development of new detection and estimation algorithms.

PASQUALE DI VIESTI (Member, IEEE) received the bachelor's and master's degrees (cum laude) in electronic engineering from the University of Modena and Reggio Emilia, Italy, in 2016 and 2018, respectively, and the Ph.D. degree in automotive for intelligent mobility from the University of Bologna, in October 2021. He is currently a Research Fellow with the University of Modena and Reggio Emilia. His main research interests include statistical signal processing and MIMO radars.

GIORGIO MATTEO VITETTA (Senior Member, IEEE) received the Dr.-Ing. (cum laude) and Ph.D. degrees in electronic engineering from the University of Pisa, Italy, in 1990 and 1994, respectively. He has been a Full Professor of telecommunications with the University of Modena and Reggio Emilia, since 2001. He has co-authored more than 100 papers published in international journals and on the proceedings of international conferences. He has co-authored the book *Wireless Communications: Algorithmic Techniques* (John Wiley, 2013). His main research interests include wireless and wired data communications, localization systems, MIMO radars, and smart grids. He has served as an Area Editor for IEEE TRANSACTIONS ON COMMUNICATIONS and as an Associate Editor for IEEE WIRELESS COMMUNICATIONS LETTERS and IEEE TRANSACTIONS ON WIRELESS COMMUNICATIONS.